JOURNAL OF PHYSICAL OCEANOGRAPHY

Geometric Constraints on Glacial Fjord-Shelf Exchange

KEN X. ZHAO*, ANDREW L. STEWART, AND JAMES C. MCWILLIAMS

Department of Atmospheric and Oceanic Sciences, University of California, Los Angeles, Los Angeles, California

ABSTRACT

The oceanic connections between tidewater glaciers and continental shelf waters are modulated and controlled by geometrically complex fjords. These fjords exhibit both overturning circulations and horizontal recirculations, driven by a combination of water mass transformation at the head of the fjord, variability on the continental shelf, and atmospheric forcing. However, it remains unclear which geometric and forcing parameters are the most important in exerting control on the overturning and horizontal recirculation. To address this, idealized numerical simulations are conducted using an isopycnal model of a fjord connected to a continental shelf, which is representative of regions in Greenland and the West Antarctic Peninsula. A range of sensitivity experiments demonstrate that sill height, wind direction/strength, subglacial discharge strength, and depth of offshore warm water are of first-order importance to the overturning circulation, while fjord width is also of leading importance to the horizontal recirculation. Dynamical predictions are developed and tested for the overturning circulation of the entire shelf-to-glacier-face domain, subdivided into three regions: the continental shelf extending from the open ocean to the fjord mouth, the sill-overflow at the fjord mouth, and the plume-driven water mass transformation at the fjord head. A vorticity budget is also developed to predict the strength of the horizontal recirculation, which provides a scaling in terms of the overturning and bottom friction. Based on these theories, we may predict glacial melt rates that take into account overturning and recirculation, which may be used to refine estimates of ocean-driven melting of the Greenland and Antarctic ice sheets.

1. Introduction

The melting at the margins of the Greenland Ice Sheet (GrIS) and Antarctic Ice Sheet (AIS) has accelerated in recent years. Near many marine-terminating glaciers in Greenland, the submarine melt rate outweighs the contribution from surface runoff (Straneo and Heimbach 2013). The postulated main cause of the recent accelerated melting of the GrIS is the warming of the East and West Greenland currents that influence the water mass properties at the termini of tidewater glaciers (Wood et al. 2018). Similar accelerated melting of the AIS is likely due to greater heat fluxes supplied to the ice shelf cavities by the Circumpolar Deep Water currents (Rignot et al. 2013; Cook et al. 2016).

In recent decades, the melting of the GrIS contributed 1 mm/yr in global sea level rise on average and this contribution is accelerating and has the potential to contribute over 7 m total (Pörtner et al. 2019). The West Antarctic Peninsula, which is a small sector of the AIS with glaciers that terminate in fjords, contributes approximately 0.2 mm/yr in global sea level rise (Pritchard and Vaughan 2007). A major implication of the accelerated ocean-driven melting of marine-terminating glaciers in these two regions is the retreat of ice sheets, which along with calving and other ice sheet processes may lead to thinning of the outward-flowing GrIS and AIS (Seroussi et al. 2011).

Fjords abutting marine terminating glaciers have also been studied in regions other than the GrIS and West Antarctic Peninsula: the Canadian Arctic Archipelago, which is occasionally grouped with the GrIS and accounts for 9% of the freshwater flux anomaly in Baffin Bay (Bamber et al. 2018); the Patagonia Ice Field (Moffat 2014); Alaska (Sutherland et al. 2019); and Svalbard (Jakacki et al. 2017). In these regions, the fjord circulation has implications for physical and biogeochemical ocean properties and potentially regional ice sheet cover and albedo, but are not important contributors to sea level rise due to the smaller ice sheet volumes.

The oceanic exchange flows between fjords and the continental shelf constrains the ocean-driven melting of the GrIS and West Antarctic Peninsula glaciers. Although progress has been made in understanding the overall sensitivity of ice sheet melt to atmospheric and oceanic forcing (see Straneo and Cenedese 2015 and references

*Corresponding author address: Department of Atmospheric and Oceanic Sciences, University of California, Los Angeles, 405 Hilgard Ave., Los Angeles, CA 90095-1565.
E-mail: kzhao@atmos.ucla.edu

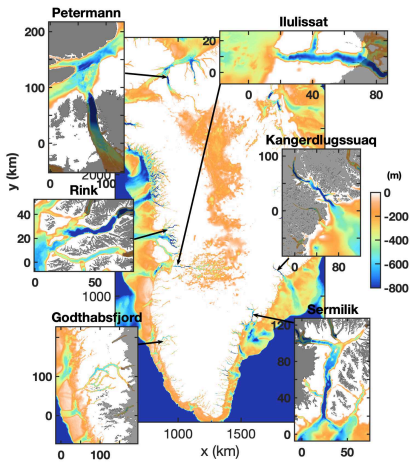

FIG. 1. Bathymetry around Greenland and zoomed-in panels of six major Greenlandic fjords with ice sheet extent (shown in gray). The data shown is from Bedmachine V3 (Morlighem et al. 2017).

therein), the translation of open ocean and fjord conditions to glacial melt rates is not well understood.

To better understand how fjords connect the open ocean to marine-terminating glaciers, recent idealized and regional modeling investigations have explored the constraints of the fjord-to-shelf circulation. Previous studies either use 2D simulations and do not account for rotational effects (e.g., Gladish et al. 2015, Sciascia et al. 2013, and Xu et al. 2012), or use 3D simulations but focus on specific processes such as winds (Spall et al. 2017), coastally-trapped waves (Fraser et al. 2018), and the wave-influenced fjord response to shelf forcing (Jackson et al. 2018). The effect of varying multiple parameters in a 3D fjord setup, e.g., sill height, tides, and wind forcing, was examined in Carroll et al. (2017). This study concluded that sill depth compared to the grounding line depth is a primary control on fjord overturning and renewal, which is amplified by both winds and tides. Carroll et al. (2017) also finds that horizontal recirculation is stronger for wider fjords, which influences the fjord stratification. However, in general, there remains a lack of theoretical constraints to predict the leading-order dynamics of fjord circulation: the fjord-to-shelf overturning circulation and the horizontal recirculation. Many of these previous numerical studies examine the sensitivity of the overturning circulation to various fjord parameters, but horizontal recirculation is rarely discussed and there are no existing theories to predict its strength.

To fill this gap, in this study we present numerical solutions of an idealized model, supported by dynamical theories of fjord-to-shelf overturning circulation and the horizontal recirculation in the fjord interior. The main difference between this study and its closest predecessor (Carroll et al. 2017) are that it allows the development of a freely-evolving shelf circulation and coastal current which interact with the fjord circulation. Including this requires our model experiments to be run for 5 years to fully equilibrate the shelf circulation and coastal current adjacent to the fjord. We also test additional parameters in the sensitivity experiments to include more parameters of leading-order importance to the fjord overturning and recirculation. This expanded exploration of parameter space allows us to develop and test simple, but comprehensive dynamical theories for the overall fjord-to-shelf overturning circulation and the horizontal recirculation in the fjord interior.

In Sect. 2, we present the model configuration and describe the setup and phenomenology of a reference simulation. In Sect. 3, we explore the dependencies of the overturning circulation and horizontal recirculation on six key geometric fjord and forcing parameters. In Sect. 4, we develop theoretical constraints for the overturning circulation/warm-water inflow in three regions of the shelf-to-glacier-face domain: the continental shelf, the fjord mouth sill, and the fjord head. Piecing together the theories of these three regions yields an overall overturning prediction in terms of the parameters explored in Sect. 3, which is supported by the simulation results. In Sect. 5, we present a theory for the recirculation strength within the fjord using the vorticity budget, which is also supported by simulations diagnostics. In Sect. 6, we discuss additional fjord phenomena observed in our simulations: the onset and effect of hydraulic control at the sill and fjord mouth, low-frequency variability manifesting as periodic fjord flushing, and high-frequency submesoscale variability in the fjord and coastal current. In Sect. 7, we discuss the major implications of including the fjord circulation in glacial melt rate estimates, summarize our findings, and provide concluding remarks.

2. Idealized Fjord-to-Shelf Model

The design of our model setup is primarily motivated by Greenland's fjords and continental shelf, but the results from the simulations are likely useful towards understanding fjord circulation in the West Antarctic Peninsula and other regions. Fig. 1 shows the bathymetry around Greenland with zoomed-in panels of bathymetry and ice-sheet extent near six major Greenlandic fjords that are amongst the most observed (Morlighem et al. 2017).

We aim to capture only a few salient geometric features in our idealized model configuration. They are often long, narrow, deep submerged glacial valleys that connect to continental shelves hundreds of meters shallower. Some fjords have a shallow sill either near the mouth of the fjord or between the fjord interior and the open ocean

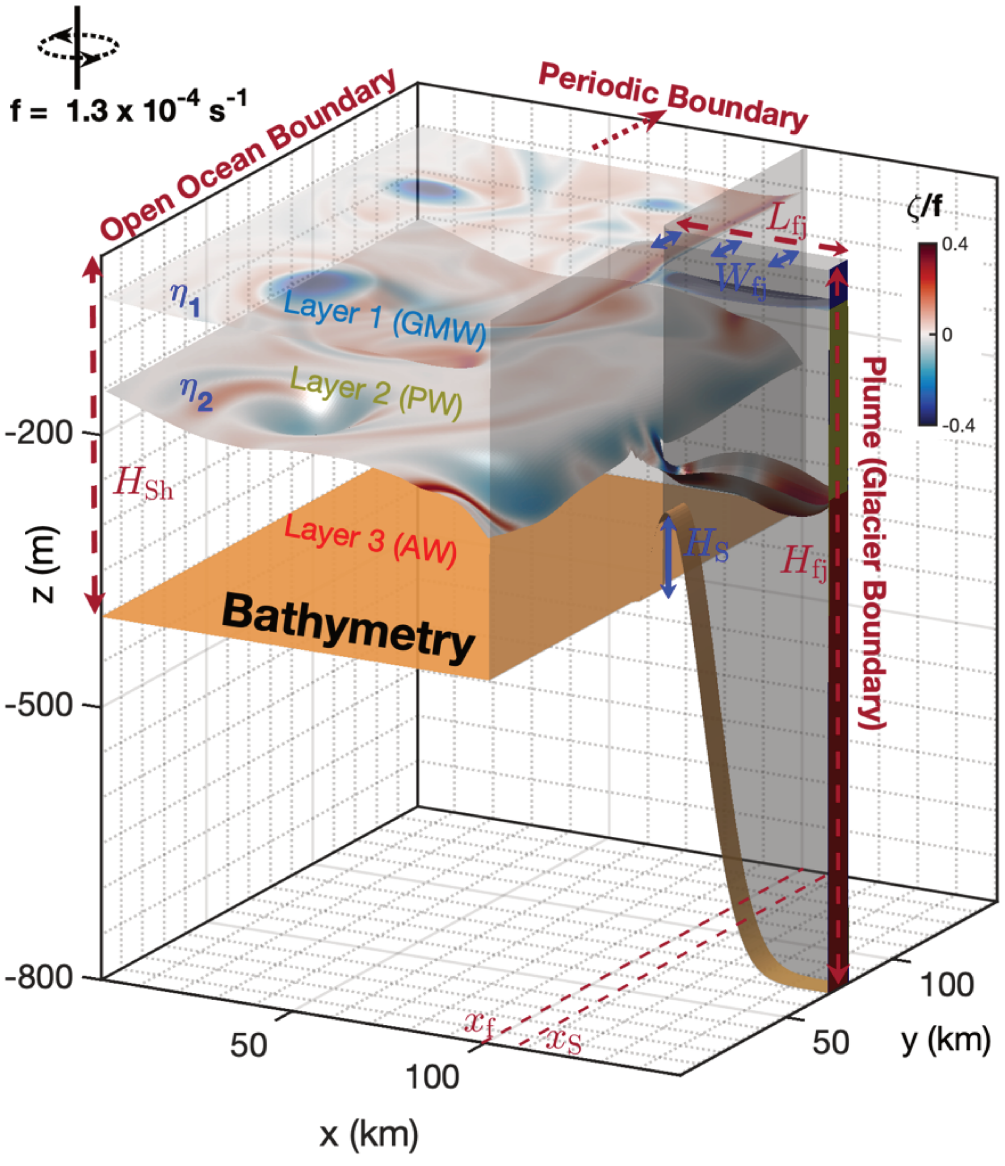

FIG. 2. Configuration and geometry of our fjord-to-shelf isopycnal model. Snapshots of middle and bottom layer vorticity are displayed on surfaces of interface depth (η_1, η_2) for the reference case with $H_S = 100$ m and $W_{fj} = 8$ km above a surface of bathymetry. The parameters in blue vary between simulations while the parameters in red are fixed. The eastern glacial boundary is coupled to a dynamic plume model which transforms water masses from denser (ρ_3 = red, Atlantic Water) to lighter water masses (ρ_2 = yellow, Polar Water, and ρ_1 = blue, Surface Water) of discrete densities.

(Ilulissat, Godthabsfjord, and Petermann are notable examples) and fjord width is typically between 2 and 20 kilometers. The coastal winds vary significantly during the year from katabatic to alongshore winds between 0 to 14 m/s (monthly averages) and 0 to 9 m/s (annual averages), which correspond to monthly-averaged wind stresses up to 0.25 N/m^2 and annual-averaged wind stress up to approximately 0.1 N/m^2 (Lee et al. 2013). Subglacial discharge exits at the base of the glacier and is generally 100s of m^3/s in the summer and nearly zero in winter (Straneo and Cenedese 2015; Chu 2014). Areas of elevated mixing within the fjord-to-shelf region are primarily forced

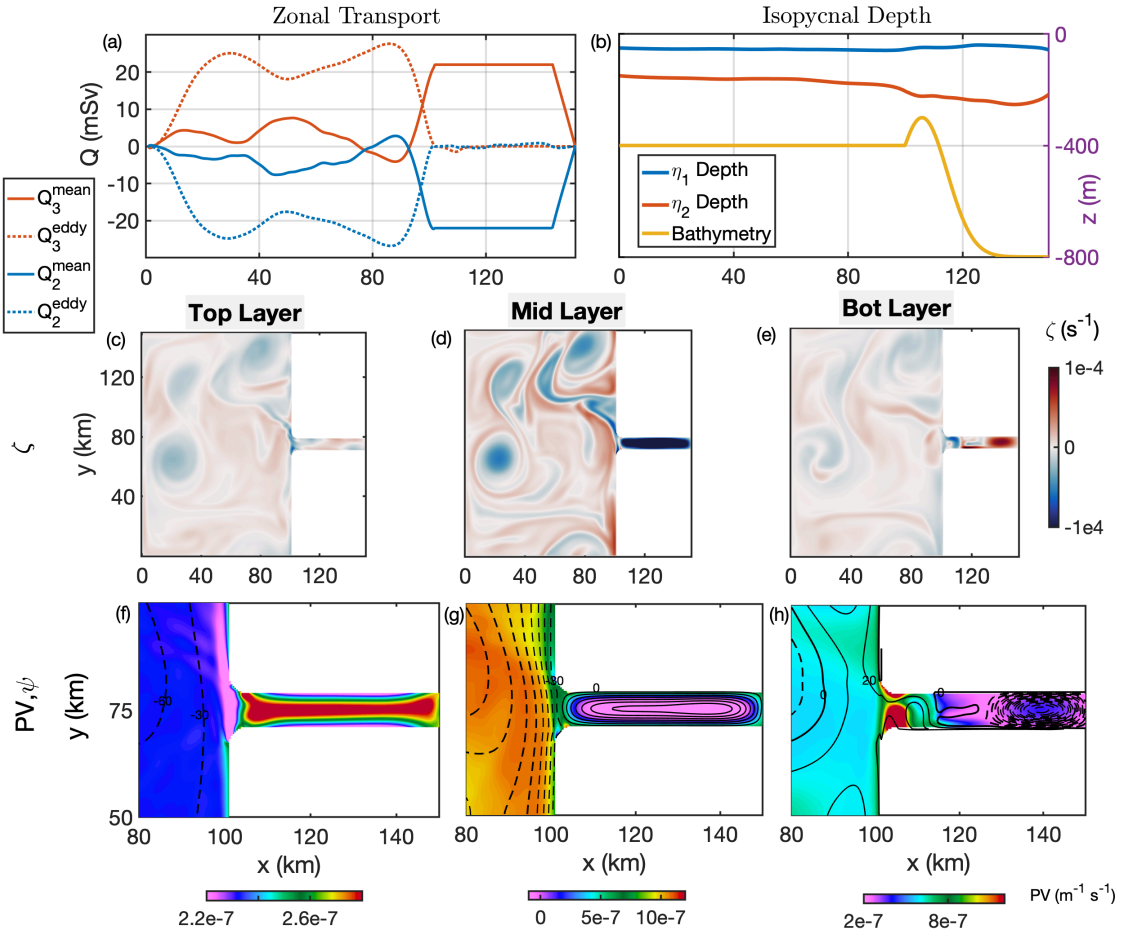

FIG. 3. Reference case simulation with H_S = 100 m and W_{fj} = 8 km. (a) Zonal transport decomposed into mean and eddy components based on Eq. (7) for the bottom and middle layer (top layer zonal transport is negligible and is therefore not shown). (b) Isopycnal interface depths η_1, η_2 and bathymetry along the midline, y = 75 km. (c)-(e) Snapshots of vorticity for each layer (at day 1600). (f)-(h) Zoomed-in PV (in color) and transport streamfunction for each layer with 30 mSv contours in top and middle layers and 20 mSv contours in bottom layer (dotted line contours are negative values). The fields in the top and bottom rows are time-averaged over days 1300 - 1600.

by subglacial and ambient melt plumes as they are a dominant mode of mixing for the majority of Greenland's fjords (Carroll et al. 2017; Gladish et al. 2015; Magorrian and Wells 2016). However, wind-driven mixing in the surface mixed layer (often shallow enough to be ignored for the interior fjord dynamics) and tidal/gravity-overflow mixing near shallow sills (which is outside the scope of this study) are also potentially important contributors.

We note that this simplified fjord-shelf configuration is not intended to fully represent the geometric complexity of Greenland's fjords, but rather to capture a few geometric features that are representative of a number of these fjords. The lack of floating ice shelves, sea ice, melange, icebergs, canyons, enclosed bays, narrow straits, remotely-generated coastal currents, etc., likely play important roles in individual fjord-shelf systems but are not captured in our simple model configuration. We do not anticipate these factors to qualitatively change our findings although they may be separately important as drivers or controls on fjord-shelf exchange (see Sect. 7 for further discussion).

a. Model Configuration

To capture key aspects of the fjord-to-shelf dynamics, we implement a 3-layer isopycnal model. With this simple model, we aim to include important elements of fjord-shelf dynamics with minimal complexity and computational cost, allowing us to conduct fully-equilibrated (5-year) simulations over a wide parameter space. The model uses 3 density layers for simplicity to represent the Atlantic layer, polar layer, and surface waters that are observed in many Greenlandic fjords (e.g. Gladish et al. 2015; Bartholomaus et al. 2016) and a 3-layer isopycnal model describes the barotropic and first two baroclinic

modes while prohibiting spurious diabatic mixing. By comparison, it has been shown that 75 well-positioned vertical layers are typically necessary to adequately resolve the first two baroclinic modes in z-coordinates (Stewart et al. 2017). Observed temperature and salinity profiles within fjords often shown three relatively unstratified layers (compared to the shelf waters), which is captured in the thicknesses of our 3 layers in a discretized and simplified way (Carroll et al. 2016).

In our model configuration, the three layers represent Atlantic Water (AW), which is warmer, saltier, and denser; Polar Water, which is colder, fresher, and lighter; and Surface Water, which is the coldest, freshest, and lightest (see Fig. 2). The fjord overturning circulation is modeled as bottom layer AW entering the fjord, which is then converted into either the middle layer Polar Water or the Surface Water layer.

We develop an idealized geometric representation of the region (see Fig. 2) from the glacier face to the open ocean (100 km offshore), which captures a few geometric features that apply to some of the Greenland fjords shown in Fig. 1. The The model domain dimensions are $W \times L \times H$ = 150 km $\times$ 150 km $\times$ 800 m. The simple model geometry consists of a flat shelf connected to a deep fjord with a Gaussian sill in the x-direction with the maximum at $x_S = 107.5$ km, which is near the fjord mouth located at $x_f = 100$ km. The bathymetric depth is

$$z_B(x) = \begin{cases} \max\{-H_{\rm Sh}, z_S(x)\}\,, & \text{if } 0 < x < x_S \text{ (shelf region)}\,, \\ z_S(x)\,, & \text{if } x_S < x < 150 \text{ km (fjord region)}\,, \end{cases}$$
$$\text{where } z_S(x) = -H_{\rm fj} + [H_{\rm S} + (H_{\rm fj} - H_{\rm Sh})] \exp(-(x-x_S)^2/L_{\rm S}^2) \tag{1}$$

The sill has a width scale $L_{\rm S} = 12.5$ km and sill height $H_{\rm S}$ (the amplitude of the sill above the shelf). The shelf has a depth of $H_{\rm Sh} = 400$ m, and is connected to a fjord of depth $H_{\rm fj} = 800$ m, length $L_{\rm fj} = 50$ km, and width $W_{\rm fj}$. Note that $H_{\rm S}$ and $W_{\rm fj}$ are the only geometric parameters varied between our experiments with ranges shown in Table 1 (see parameter sensitivity discussion in Sect. 3). The shelf is 100 km wide in the across-shelf direction (x) and 150 km long in the along-shelf direction (y) and is periodic in y. The across and along-shelf length scales are fixed and chosen to represent the width of a continental shelf and the choice of a periodic domain represents an average inter-fjord separation distance (approximately 100 to 150 km between one fjord to the next in Fig. 1).

The lateral side boundaries of the fjord and coastline are represented as vertical walls due to the horizontal resolution limiting realistic coastal slopes to span only 2-3 horizontal gridpoints (1 km), i.e. a bathymetric steepness of 1/2 near the six fjords in Fig. 1 (Morlighem et al. 2017). At coarse resolution, such under-resolved coastal slopes would produce spurious results in the boundary currents that emerge. A high-resolution near-fjord configuration with a smaller shelf was tested with both vertical walls and varying side slope steepness (1/4 to 1, not shown) without significant variation in boundary current transport. Using 90$^{\rm o}$ corners at the fjord mouth led to large, spurious sources of vorticity, so we replaced them with quarter-circular rounded corners with radii of 3 km. We also experimented with a continental shelf slope of width 5 km and steepness 1/10 positioned at $x = 0$ (i.e., extending the Fig. 2 domain 20 km offshore to include a shelf and flat deep bathymetry), but found that this did not significantly alter our results.

b. Model Equations

We use the Back of Envelope Ocean Model (BEOM), which is a publicly available code (St-Laurent 2018). BEOM is a hydrostatic shallow-water isopycnal model with a nonlinear free surface that simulates rotating basins and allows for layer-outcropping.

We pose our problem as a 3-layer exchange flow over bathymetry on an f-plane using shallow-water momentum and continuity equations

$$\frac{\partial \mathbf{u}_n}{\partial t} + (\mathbf{u}_n \cdot \nabla)\mathbf{u}_n + f\hat{\mathbf{z}} \times \mathbf{u}_n = -\nabla \phi_n + \boldsymbol{F}_{{\rm wind},n} - \boldsymbol{F}_{{\rm fric},n} + \upsilon \mathbf{S}_n\,, \tag{2a}$$

$$\frac{\partial h_n}{\partial t} + \nabla \cdot (h_n \mathbf{u}_n) = \varpi_n\,, \tag{2b}$$

for layers n = 1, 2, 3. Here, u is the zonal velocity (in the x-direction), v is the meridional velocity (in the y-direction), and the top, middle, and bottom layer thicknesses are h_1, h_2, and h_3. We parameterize the water mass transformation as ϖ, surface and bottom boundary stresses as $\boldsymbol{F}_{\rm wind}$ and $\boldsymbol{F}_{\rm fric}$, and eddy viscosity as $\upsilon\mathbf{S}$. We use an f-plane approximation with a representative Coriolis parameter of $f = 1.31 \times 10^{-4}\, s^{-1}$ corresponding to latitudes in central Greenland.

The water mass transformation between the layers occurs at the western (open-ocean) and eastern (plume parameterization) boundaries and is defined as

$$\varpi_n = \begin{cases} -\tau_h^{-1}(h_n - H_n^W), & \text{for } \mathbf{x} \in A_W\,, \\ \varpi_{n,{\rm p}}, & \text{for } \mathbf{x} \in A_E\,, \\ 0, & \text{otherwise.} \end{cases} \tag{3}$$

In the 10 km-wide nudging region at the western boundary, A_W, each layer n is restored to H_n^W with a nudging strength $\propto \tau_h^{-1}$ for a timescale $\tau_h = 1$ day that decreases linearly to zero in the interior edge of the nudging zone. At the eastern boundary, we parameterize the time-evolving plume-driven water mass transformation as $\varpi_{n,{\rm p}}$ using a point plume model (Turner 1979) applied to the 3-layer density stratification (see Appendix A for the details). We

also implemented a line plume parameterization of variable width in our model, which exhibits negligible differences in the water mass transformation for small plume source widths (further discussed in Appendix A). We assume in our model setup that all of the diabatic forcing occurs at the western and eastern boundary and exclude mixing within the domain due to tides and sill overflows.

A wind stress of $\boldsymbol{F}_{\text{wind},n} = \boldsymbol{\tau}/(\rho_n h_n)$ is imposed in the highest layer n with non-negligible thickness ($h_n >$ 0.5 m) with $\boldsymbol{\tau} = (\tau_x, \tau_y)$. Bottom friction is parameterized by a quadratic drag $\boldsymbol{F}_{\text{fric},n} = C_d {h_n}^{-1} |\mathbf{u}_n| \mathbf{u}_n$ with $C_d = 2.5 \times 10^{-3}$ and only acts in the lowest layer n with non-negligible thickness ($h_n > 0.5$ m). In numerical calculations, we control grid-scale energy and enstrophy using a thickness-weighted biharmonic eddy viscosity term $\upsilon \mathbf{S}_n$, for which $S_n^x = h^{-1}[\partial_x(hF^x) + \partial_y(hF^y)]$, $S_n^y = h^{-1}[\partial_x(hF^y) - \partial_y(hF^x)]$, where $F_n^x = \partial_x \nabla^2 u_n - \partial_y \nabla^2 v_n$, $F_n^y = \partial_x \nabla^2 v_n + \partial_y \nabla^2 u_n$ (Griffies and Hallberg 2000). The Montgomery potential is defined as

$$\phi_1 = g\eta_0\,, \tag{4a}$$

$$\phi_2 = g\eta_0 + g'_{3/2}\eta_1\,, \tag{4b}$$

$$\phi_3 = g\eta_0 + g'_{3/2}\eta_1 + g'_{5/2}\eta_2\,, \tag{4c}$$

where η_0 is the free surface elevation. The reduced gravity at the two interfaces η_1 and η_2 are

$$g'_{3/2} = g(\rho_2 - \rho_1)/\overline{\rho}\,, \tag{5a}$$

$$g'_{5/2} = g(\rho_3 - \rho_2)/\overline{\rho}\,, \tag{5b}$$

as defined by the layer interface depths $\eta_1 = \eta_0 - h_1$ and $\eta_2 = \eta_0 - h_1 - h_2$. The reference densities (chosen based on Ilulissat conditions from Gladish et al. 2015) for the three layers are $(\rho_1, \rho_2, \rho_3) = (1025.5, 1026.5, 1027.0)$ kg/m^3, but varying stratification is also explored in Sect. 3. This choice of stratification corresponds to a reduced gravity at the two interfaces of $g'_{3/2} = 9.6 \times 10^{-3}$ m^2/s and $g'_{5/2} = 4.8 \times 10^{-3}$ m^2/s.

Throughout this study, we use an internal baroclinic deformation radius defined as

$$L_{\text{d}}(h_2, h_3) = \left(\frac{g'_{5/2} h_2 h_3}{f^2 (h_2 + h_3)} \right)^{1/2}, \tag{6}$$

which only takes into account the stratification of the bottom two layers because the uppermost layer is typically negligibly thin in most of our simulations. To adequately resolve the transport of a L_{d}-wide boundary current, we use a horizontal resolution of dl = 400 m all of the runs discussed (except for the dl = 68 m experiment discussed in Sect. 6). We find that L_{d} based on h_2 and h_3 evaluated at the sill maximum ($x = 107.5$ km) is a useful approximation for the boundary current width due to the sill's role in establishing the boundary current width. We use a time step of 100 s and simulations are run for 1600 days to reach a statistically steady state, which is measured by the domain-integrated available potential energy. This duration is required to fully spin up the shelf circulation and coastal current, which influences the dynamics within the fjord.

The 3-layer setup is more advantageous than a 2-layer setup primarily because the plume parameterization in three layers allows a partition of the exiting water masses between the top two layers, which serves as a proxy for exiting plume depth. By comparison, the 2-layer setup has no way of specifying the exiting plume depth since all of the bottom layer inflow must exit as outflow in the top layer. Moreover, this degree of freedom provided by a 3-layer setup is critical for the implementation of the plume parameterization since the overturning circulation in a 2-layer setup can be determined entirely by the density of the two layers and the rate of subglacial discharge via the Knudsen relations. However, a 3-layer setup must take into account the plume density and its level of neutral buoyancy, which provides a more physical control of the plume on the overturning circulation (see Appendix A for further discussion). Another implication for using three layers is that the overturning between the bottom two layers is allowed to realistically transition to an overturning between the top two layers, which results in a substantially decreased heat transport since the middle layer has significantly less available heat content than the bottom layer. Although our isopycnal model does not carry a temperature variable, onshore heat transport inferences can be made by assigning realistic potential temperatures to each of the three density classes. In Greenland's fjords, the lower layer has typical potential temperatures of 2 to 4 $^{\text{o}}$C, while the middle and top layers are within the range of -1 to 1 $^{\text{o}}$C, which is why the bottom layer inflow is particularly important.

The goal of our choice to specify the boundary conditions (wind stresses, subglacial discharge rate, and open-ocean stratification) to be constant with time is to better understand the fully-equilibrated shelf-to-fjord mean circulation. While it is true that this constant forcing does not represent the full reality of Greenland's fjords, we believe it to be a necessary step before considering the superimposed effects of variability on the system, which is further discussed in Sect. 6.

c. A Reference Case

Diagnostics from a reference case simulation with sill height $H_{\text{S}} = 100$ m and fjord width $W_{\text{fj}} = 8$ km are shown in Fig. 2. Snapshots of the middle and bottom layer vorticities are mapped onto the isopycnal interface depths η_1 and η_2. The reference case parameters are selected based on conditions in Ilullisat Icefjord in West Greenland (Gladish et al. 2015) and are intermediate values for the

parameter space explored in the sensitivity experiments in Sect. 3.

In Fig. 3, we present a series of diagnostic fields that capture the dynamics of this reference case including the time-mean zonal transport and isopcynal gradients, instantaneous vorticity fields showing mesoscale eddies on the shelf, and the fjord-focused circulation using time-averaged potential vorticity (PV) and transport streamfunction. Nearly all of the features in this reference case are observed in the series of parameter sensitivity simulations discussed in Sect. 3.

In Fig. 3a, we show the meridionally-integrated zonal transport decomposed into mean and eddy components, defined as

$$Q_n = \int \overline{h_n u_n}\,\mathrm{d}y = \underbrace{\int \overline{h}_n \overline{u}_n\,\mathrm{d}y}_{Q_n^{\mathrm{mean}}} + \underbrace{\int \overline{h_n' u_n'}\,\mathrm{d}y}_{Q_n^{\mathrm{eddy}}}. \tag{7}$$

The total transport is inflowing (towards the fjord) in the bottom layer and outflowing (away from the fjord) in the middle layer. The zonal transport is dominated by eddies on the shelf with a small contribution of mean transport due to eddy momentum flux convergence (not shown) and dominated by mean flow primarily via boundary currents in the fjord interior. The midline ($y = 75$ km) isopycnal interface depths highlight the across-shelf pressure gradient in the middle and bottom layer (particularly those near the fjord mouth), which drives a baroclinic coastal current that is weaker/southward in the bottom layer and stronger/northward in the middle layer.

The vorticity snapshots for each layer in Fig. 3c-e show eddies shedding from the fjord mouth and coastal current primarily via baroclinic instability, which depends on the zonal isopycnal/pressure gradient. This is diagnosed using the same analysis as Zhao et al. 2019, which in this case shows the eddy energy production is dominated by conversion from potential energy rather than kinetic energy (not shown). These eddies are the dominant mode of transport across the y-periodic shelf. However, the peak in vorticity is located in the middle and bottom layer steady recirculation within the fjord and is connected to the overturning circulation via the bottom layer boundary current and middle layer coastal current.

Fig. 3f-h shows a zoomed-in view of the fjord interior transport streamfunction and PV for each layer, which are defined as

$$\overline{h_n \mathbf{u}_n} = (-\partial_y \psi_n, \partial_x \psi_n), \tag{8a}$$

$$q_n = (f + \zeta_n)/h_n. \tag{8b}$$

Note that the streamfunction is not well-defined in the eastern and western diabatic boundaries due to the divergence of the time-mean mass flux in each layer, so we set $\psi = 0$ at the northern fjord wall and integrate meridionally across the fjord to determine ψ throughout the fjord, and then integrate zonally across the shelf (i.e., using a path of integration that avoids diabatic regions for the non-diabatic interior).

In the bottom layer streamfunction, the southward coastal current enters the fjord via a boundary current, which initially flows retrograde (with the boundary to the left of the flow) along the northern boundary of the fjord. The flow crosses the channel on the eastern side of the sill maximum since topographic beta, $\beta_{\mathrm{topo}} = -f\partial_y(z_B)/h_3$, changes sign due to a reversal of the bathymetric slope. In this case, the flow crossing occurs at $x = 114$ km, which is diagnosed using the 20 mSv contour in Fig. 3h. The sill establishes a PV barrier in the bottom layer, which appears as a red patch in the PV field. The 20 mSv transport streamfunction illustrates the transport pathway approximately following PV-isolines, which serve as barriers that guide the flow. The boundary current then feeds the gyre-like recirculation in the deeper fjord interior, where it is converted into the middle layer water mass by the diabatic plume-driven water mass transformation. The flow in the middle layer recirculates with a small fraction flowing back out towards the open ocean via eddy transport across the shelf.

The recirculation in the middle layer is slightly weaker than the bottom layer and extends the length of the fjord since it is effectively unconstrained by bathymetry. Compared to the bottom layer, the bathymetry exhibits a much weaker influence on the top and middle layers. We quantify the recirculation using the streamfunction extrema within the fjord as

$$\psi_r = \max_{100<x<150\ \mathrm{km}} (|\psi_n|), \tag{9a}$$

which is ∼200 mSv in the middle layer and ∼300 mSv in the bottom layer — an order of magnitude larger than the overturning circulation.

3. Parameter Dependencies

The reference case motivates us to seek an understanding for the parameter dependencies of the two bulk fjord circulation properties: the overturning circulation and horizontal recirculation. The overturning and recirculation control parameters can be classified into geometric, forcing-related, and stratification, and our goal is to test the sensitivity of a few simple parameters that to first order capture the parameter variations amongst Greenland's fjords.

Although various complex geometric controls can exist (bends in the fjord, non-uniform fjord width, shelf troughs, multiple sills, etc.), we anticipate that the features of first-order importance to the overturning are sill height, H_{S}, and fjord width, W_{fj}, which act to horizontally and vertically constrict the exchange flow at the fjord mouth. Forcing parameters that are of first-order importance to the fjord-shelf exchange are wind direction and strength, subglacial

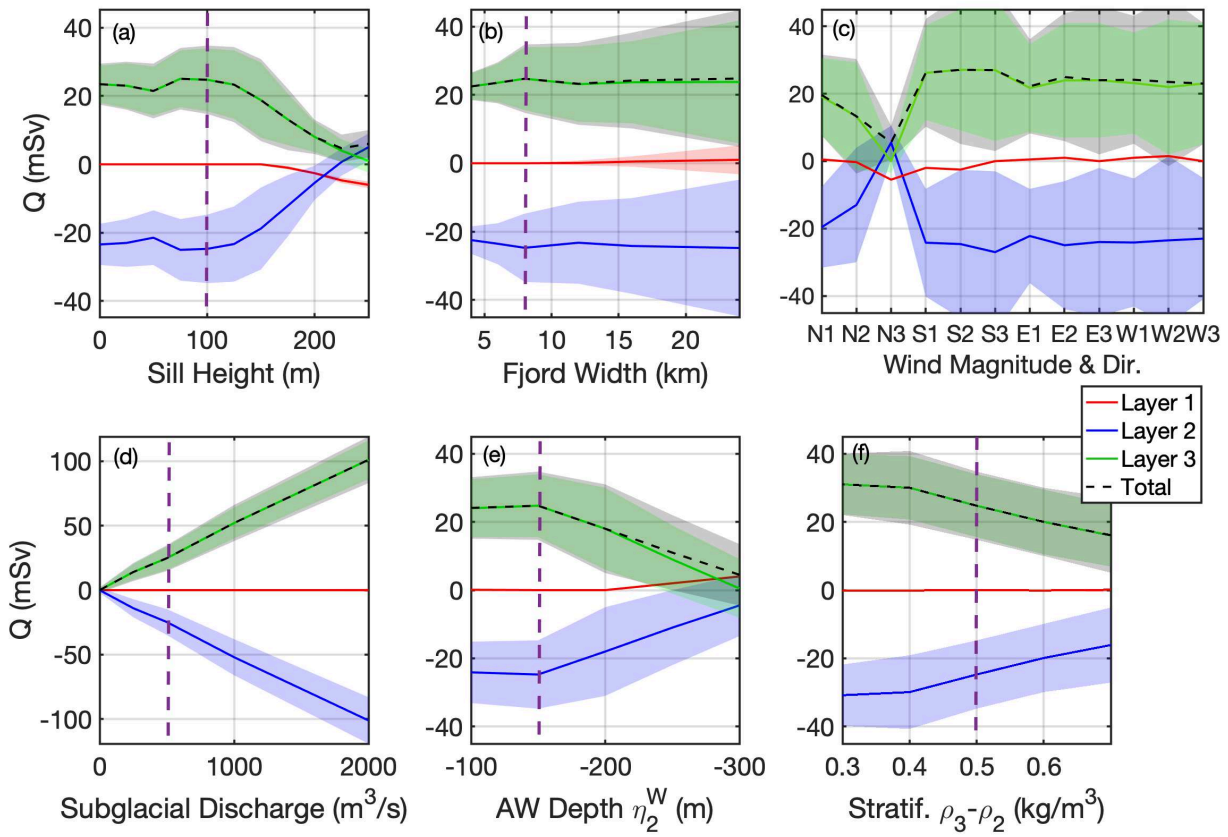

FIG. 4. (a)-(f) Time-averaged (days 1300-1600) mean transport for each layer n based on Eq. (7) diagnosed at the sill maximum ($x = 107.5$ km) and its root-mean-square deviation (color shading denotes positive and negative values calculated from the timeseries for each respective case). Transports are positive toward the glacier. The purple dotted line shows the parameter choice of the reference case (from Figs. 2 and 3). The wind magnitude is [N1, N2, N3] = [0.015, 0.03, 0.1] N/m^2 and similarly for the other wind directions in panel (c).

discharge strength, and open ocean boundary conditions, which we quantify as AW depth, η_2^W. Some of these parameters have been tested previously in modeling results (Carroll et al. 2017; Gladish et al. 2015), and are known to influence the dynamics of the continental shelf, the fjord mouth sill, and the fjord head regions (Straneo and Cenedese 2015).

Therefore, we choose to vary the following six parameters: sill height, fjord width, wind direction/strength, subglacial discharge strength, AW depth, and stratification. The key parameters and test cases are listed in Table 1, with parameter variations selected to span the range of existing glacial fjord measurements.

a. Summary of Dependencies

Fig. 4a-f shows the sensitivity of the overturning circulation and its root-mean-square deviation (RMSD) to each of the six parameters. Relative to the reference case, the overturning circulation varies most significantly with sill height, AW depth, winds, and subglacial discharge over realistic parameter variations.

For tall enough sills (H_S above 150 m), deeper AW ($\eta_2^W + H_{Sh} \approx H_S$), and strong northward winds, the outflow transitions from the middle to the top layer (red line in Fig. 4a,e). In such cases, the plume density is light enough to rise past the middle layer and exit via the top layer due to a thin bottom layer water mass that is only weakly entrained by the plume. Here, the AW depth at the western boundary η_2^W increases as the bottom layer thickness $H_3^W = H_{Sh} + \eta_2^W$ decreases. This transition of the overturning circulation between the bottom two layers to the top two layers for high sill cases as well as greater AW depth or stronger downwelling-favorable winds is seen in Fig. 4a,c,f and is further discussed in Appendix A. Although large H_S, deeper AW, and small Q_0 can each lead to the complete shutoff of warm AW (bottom layer) transport toward the fjord, denoted as Q_3, it is also plausible that a weak enough stratification between the bottom and middle layers ($\sim$0.1 kg/m^3 or less) or a small enough fjord width

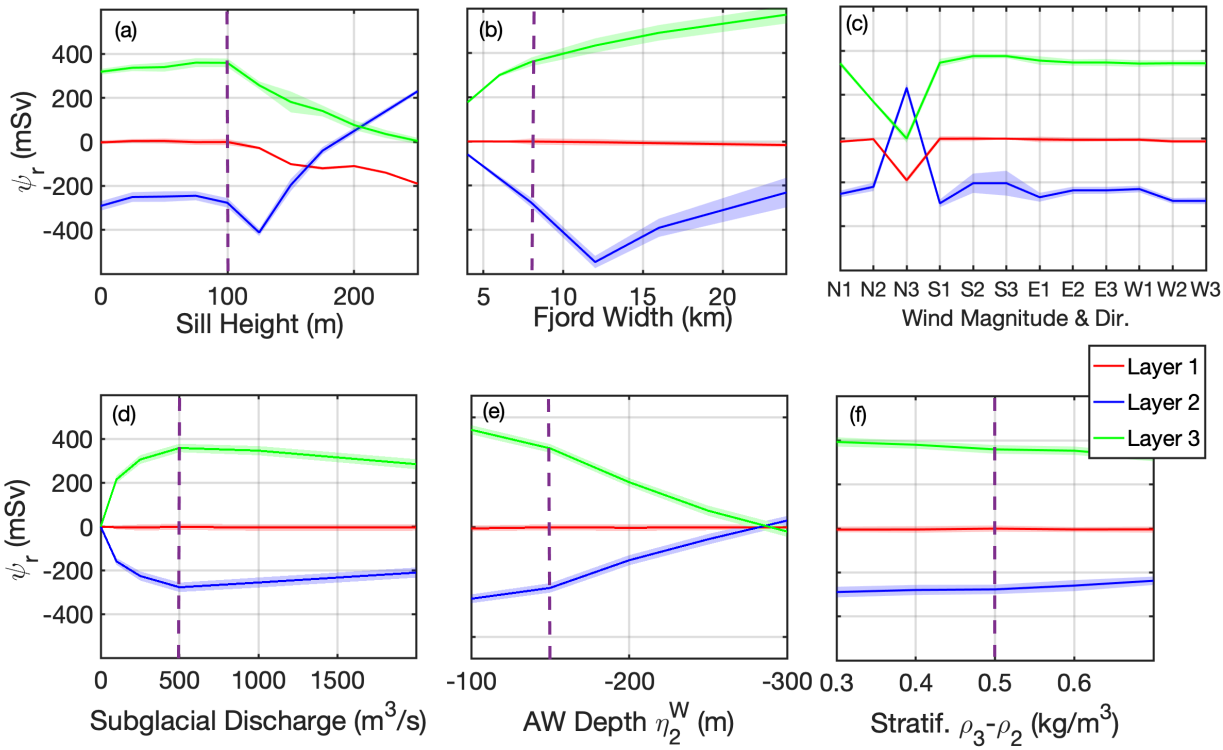

FIG. 5. (a)-(f) Time-averaged (days 1300-1600) recirculation strength ψ_r (diagnosed as the streamfunction extremum using Eq. (9a)) within the fjord in each layer, where positive values correspond to cyclonic circulation. Recirculation root-mean-square deviation is shown with color shading (calculated from the timeseries for each respective case). The purple dotted line shows the parameter choice of the reference case (from Figs. 2 and 3). The wind magnitude is [N1, N2, N3] = [0.015, 0.03, 0.1] N/m^2 and similarly for the other wind directions in panel (c).

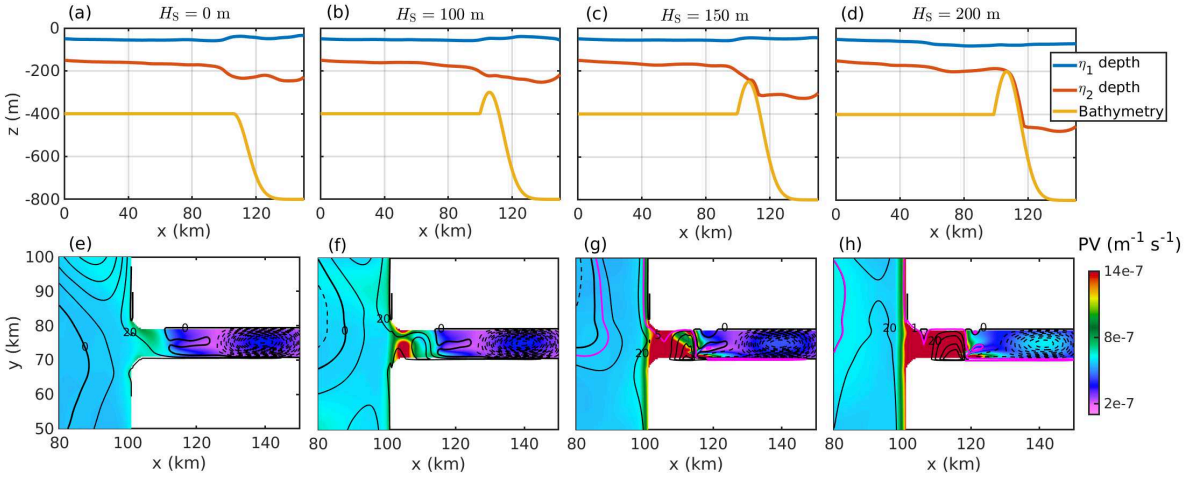

FIG. 6. (a)-(d) Side profile depths of η_1, η_2, and bathymetry along midline (y = 75 km); and (e)-(h) zoomed-in bottom layer PV (in color) and transport streamfunction using 20 mSv contours for four cases of varying sill height. The dotted line contours show negative values and additional pink contours in panels g and h highlight the fjord-shelf connectivity. All fields are time-averaged over days 1300 - 1600.

(1 km or less) may also lead to weakened heat transport into the fjord.

Similarly to Fig. 4 for overturning sensitivity, Fig. 5a-f shows the dependency of horizontal recirculation on the

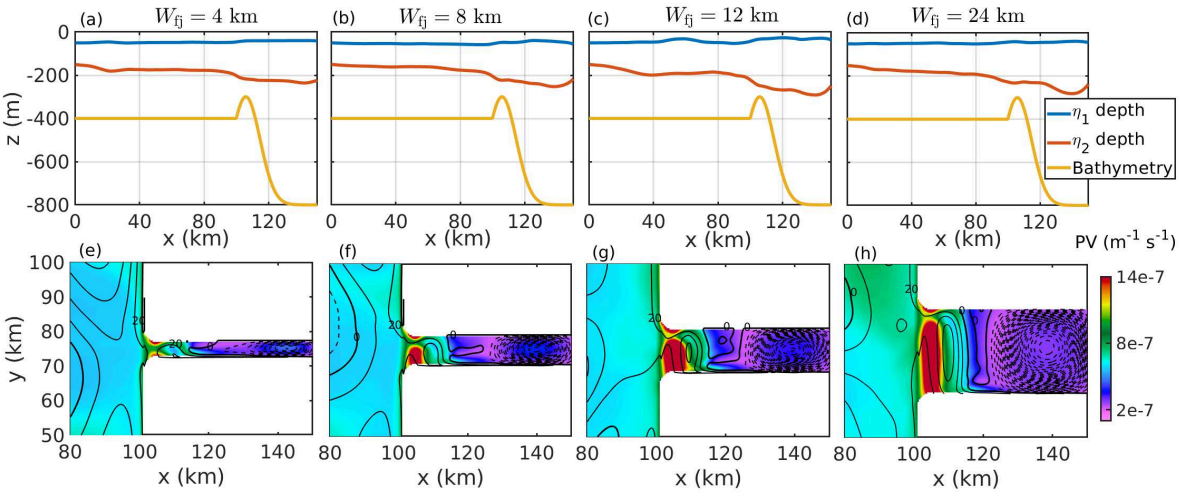

FIG. 7. Same as Fig. 6 for four cases of varying fjord width.

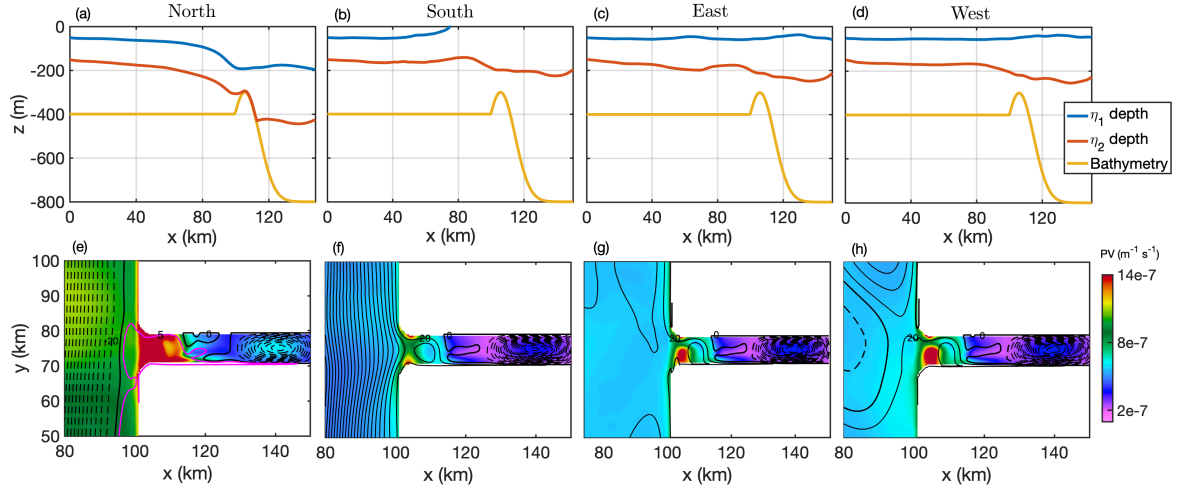

FIG. 8. Same as Fig. 6 for four cases of varying wind direction with constant magnitude 0.03 N/m^2. An additional pink contour in panel e highlights the fjord-shelf connectivity for the northward wind case.

same six parameters. The recirculation in the bottom/AW layer, which is the most important due to its lateral heat transport to the glacier face, varies primarily with sill height, fjord width, subglacial discharge, and AW depth. If we compare the recirculation sensitivity in each layer with the overturning circulation sensitivity in Fig. 4, we see approximately the same trends for sill height, winds, η_2^W, and stratification. However, the sensitivity of recirculation to fjord width in Fig. 5b is visibly higher than for overturning in Fig. 4b. For discharge strength shown in Fig. 5d, the recirculation saturates near $Q_0 = 500$ m^3/s while the overturning continues to linearly increase in Fig. 4d. The middle layer recirculation approximately opposes the recirculation in the bottom layer, except for cases of wide fjords or nonzero top layer recirculation (especially in tall sill cases).

We now discuss the parameter sensitivity of the fjord dynamics in greater detail and describe the flow behavior in response to these key parameter variations.

b. Sill Height and Fjord Width

Fig. 6a-d shows the time-averaged isopycnal depth variations along the y-midline and panels e-h shows the bottom layer PV and transport streamfunction for four cases of varying sill height. As discussed in the reference case (Fig. 3), a common feature is the coastal current, which flows southward in the bottom layer and enters the fjord as a narrow L_d-wide boundary current. The boundary current

flows along and across the fjord and subsequently feeds a cyclonic recirculation gyre in the fjord interior.

The interface depth in Fig. 6a-d shows a transition from a 100 m zonal η_2 difference ($\eta_2^{\mathrm{W}} - \eta_2^{\mathrm{E}}$) in the no-sill case (Fig. 6a) to a significantly larger 300 m difference for the $H_{\mathrm{S}} = 200$ m case in Fig. 6d, with the bottom layer nearly grounded on the sill bathymetry. The bottom layer thickness inside the fjord decreases by approximately a factor of 2 between the $H_{\mathrm{S}} = 0$ and the $H_{\mathrm{S}} = 200$ m cases.

In Fig. 6e-h, the time-averaged PV and transport streamfunction also show a noticeable change in the fjord-shelf connectivity via the coastal and boundary current for taller sills. The sill establishes a PV barrier in the bottom layer, which appears as a red patch in the PV for cases with sills. In the $H_{\mathrm{S}} = 0$ case, the PV barrier is weak and the streamfunction shows that the flow from the coastal current crosses the fjord gradually to join the boundary current and recirculation gyre. For taller sills, the boundary current enters as a narrower boundary current with weaker transport (outlined in a pink contour in panels g and h). In these cases, the isopycnal structure is suggestive of a hydraulically-controlled exchange flow (Pratt and Whitehead 2007), discussed further in Sect. 4. An anticylonic recirculation develops on the downstream side of tall sills and the bottom layer recirculation weakens for the tallest sills due to decreased overturning strength and the bottom friction acting on a decreased bottom layer thickness (further discussed in Sect. 5).

Fig. 7a-h shows plots of isopycnal depth, bottom layer PV, and transport streamfunction for varying fjord width. In Fig. 7a-d, interfacial depths of η_2 along the y-midline show a $\sim$10% increase in zonal η_2 differences between $W_{\mathrm{fj}} = 4$ to 24 km, which is consistent with the minimal increase in overturning circulation for wider fjords shown in Fig. 4b. However, the bottom layer recirculation strengthens by $\sim$80% between the 4 km and 8 km case and $\sim$60% between the 8 km and 24 km cases. Depressions in the isopycnal depths due to the strength of the opposing gyre recirculation in the bottom and middle layers are more clearly observed for the wider fjords, e.g. Fig. 7c,d. In these cases, a weak recirculation of $\sim$20 - 40 mSv also develops over the sill. Regardless of fjord width, we see the flow consistently entering the fjord through an L_{d}-wide current in the northern boundary, which appears visually in the PV field as a small trough in the near-sill PV barrier in Fig. 7e-h. Although the narrow fjord widths cases are limited by horizontal resolution, fjord-only test cases (not shown) suggest a reduction in overturning and larger zonal isopycnal gradients for fjords narrower than L_{d}.

c. Wind Strength and Direction

Wind stress magnitudes of τ = [0.015, 0.03, 0.1] N/m^2 were tested (corresponding approximately to a range of 3.5 to 9 m/s wind velocities), which are fairly representative of the annual average winds along the Greenland coast and not of shorter-term extremes (Lee et al. 2013). The resulting y-midline depths of η_1 and η_2 are shown in Fig. 8a-d and time-averaged bottom layer PV and transport streamfunction in panels e-h for four cases of varying wind direction and wind stress magnitude $\tau = 0.03$ N/m^2.

The eastward and westward wind cases did not change the mean state appreciably, but the northward and southward cases visibly tilt both isopycnals (through Ekman transport) in Fig. 8a,b leading to a zonal isopycnal depth change of $\Delta\eta_2 = -190$ m and $\Delta\eta_1 = -150$ m for northward winds, and $\Delta\eta_2 = 50$ m and $\Delta\eta_1 = 50$ m for southward winds. For the northward wind case shown, 80% of the zonal gradient in η_2 occurs on the shelf and the bottom layer is $\sim$200 m thinner in the fjord interior than the eastward/westward wind cases.

The streamfunctions in Fig. 8e,f show an inflow that is significantly weaker in the northward wind case and slightly stronger in the southward wind case compared to the eastward and westward wind cases (Fig. 8g,h). This is influenced by the bottom layer coastal current supplying the fjord overturning, which changes from a weak southward transport of $\sim$40 mSv in the reference case (in Fig. 3) to a $\sim$200 mSv northward transport for northward winds, $\sim$500 mSv southward transport for the southward wind case, $\sim$40 mSv (no change) for the eastward wind case, and $\sim$20 mSv northward transport for the westward wind case. Due to the thin bottom layer thickness above the sill for the northward wind case, there is a strong PV barrier (similar to the tall sill cases) for the northward wind case and a reduced barrier for the southward winds.

The sensitivity of the fjord dynamics to northward winds via differences in the isopycnal depths, coastal current strength, and meridional profile of the inflow lead to a 45% reduction in overturning and 40% reduction in recirculation for the intermediate wind case (0.03 N/m^2) and a complete shutoff of both the overturning and recirculation for the highest northward wind case (0.1 N/m^2). These results show northward winds are the most important in reducing the overturning and recirculation and is likely to be even more significant for fjords with weaker plume-driven overturning where the Ekman transport contribution is comparatively larger.

Our wind tests use time-constant winds that are uniform over the whole domain and are intended to capture the influence of steady winds on shelf circulation (upwelling and downwelling) and its influence on mean fjord circulation. We use annual-mean winds since the shelf circulation and across-shelf transport requires years to spin up, while seasonal winds may likely lead to strong, but transient controls on fjord-shelf exchange. In this setup, a strong northward wind (0.1 N/m^2) was sufficient to completely shut off the warm AW transport due to a vanishing

bottom layer near the fjord mouth with strong eddies dominating the shelf, which in practice may be dampened by bathymetric features on the shelf.

Although it is likely that time-varying winds are equally or more important than the annual-mean winds, we have only included the annual-mean wind effects as a starting point for assessing the role of winds on fjord-shelf exchange in this study. A more realistic time-varying wind forcing including shorter timescale extreme events are likely to excite coastally-trapped waves and other modes of variability as well as non-equilibrium rapid flushing events (e.g., Spall et al. 2017), which are not considered in this study and require further exploration.

d. Subglacial Discharge, AW Depth, and Stratification

Of the parameters tested, subglacial discharge has the most predictable effect on overturning strength (as shown in Fig. 4d), which increases linearly with discharge along with a moderate increase in transport RMSD. This is unsurprising given the theory of diabatic plume forcing in Appendix A implemented in the eastern boundary condition. Increasing the overturning circulation via subglacial discharge from 0 to 100 mSv strengthens the boundary current from $\sim$0 to 100 mSv, coastal current from $\sim$0 to 300 mSv, and recirculation in the middle and bottom layers from $\sim$0 to 300 mSv (which saturates near $Q_0 = 500$ m^3/s). The strength of the recirculation and overturning is likely dependent on the grounding line depth (level of subglacial discharge), which is a parameter we do not vary.

Varying the AW depth at the western boundary η_2^{W} is found to have nearly the same effect as varying the sill heights, i.e. decreasing η_2^{W} from -100 m to -300 m had approximately the same effect as increasing H_{S} from 0 m to 250 m (see Fig. 4a,e). This is unsurprising since the nondimensionalized sill height, $H_{\mathrm{S}}/H_3^{\mathrm{W}}$, varies inversely with $H_3^{\mathrm{W}} = H_{\mathrm{Sh}} + \eta_2^{\mathrm{W}}$ and represents the importance of sill height in constraining the overturning circulation. Additionally, in Fig. 5e, the recirculation within each layer is proportional to the overturning and follows the same trend.

Increasing stratification (i.e., increasing $\rho_3 - \rho_2$ from 0.3 to 0.7 kg/m^3) has the effect of decreasing the overturning circulation from 30 mSv to 17 mSv (shown in Fig. 4f), which, similarly to the other parameters, led to increases in the recirculation and coastal current albeit with much weaker trends (10% increase over the range of stratification). The effect of stratification on fjord dynamics in the context of plume theory is further discussed in Appendix A.

4. Overturning Circulation

Following the results from the sensitivity studies, we develop theories to predict the overturning circulation as a function of the parameters explored in Sect. 3. For simplicity, we focus on the AW inflow in the bottom layer, Q_3, since it is nearly proportional to the heat flux towards the glacial face and the most important transport for melt rate estimates (e.g., Inall et al. 2014).

We present and assess theories for the transport across each of the three regions: the continental shelf, the fjord mouth sill, and the fjord head. We first discuss the continental shelf region with an across-shelf transport, Q_{shelf}, primarily driven by eddies and Ekman transport. We then discuss the fjord mouth sill region with a sill-overflow transport, Q_{fjord}, which admits both geostrophic and hydraulically-controlled transport predictions (based on the theory from Zhao et al. 2019). Following this, we discuss the fjord head region with a diabatic water mass transformation, Q_{plume}, driven by plume entrainment at the glacier face. This diabatic water mass transformation in the steady state is balanced by the diabatic transport at the western boundary and due to the restoring, this transport must match the other transports and is not included in the theory.

In the following subsections, we use diagnosed bottom layer thicknesses at the fjord mouth H_3^{f} and at the glacier boundary H_3^{E}) to test the theoretical transport estimates, and then combine these estimates to develop a prediction for the isopycnal depths in each region and the overall transport. A schematic showing the zonal overturning circulation and relevant definitions is shown in Fig. 9a.

a. Across-Shelf Transport

The bottom layer across-shelf transport Q_{shelf} is the sum of both eddy and mean contributions. We first discuss the eddy transport in the absence of winds and then discuss the mean Ekman transport.

In Fig. 3, the zonal transport for the reference case (with no winds) shows that the across-shelf eddy thickness fluxes driven by the zonal isopycnal difference dominate the total transport. We can use the conventional downgradient assumption applied to eddy thickness fluxes to derive the across-shelf eddy transport (e.g., Gent and McWilliams 1990). The eddy transport from the open ocean to the fjord mouth is described by

$$Q_{\mathrm{eddy}} = \kappa W (H_3^{\mathrm{W}} - H_3^{\mathrm{f}})/L_{\mathrm{Sh}}\,, \tag{10}$$

where $W = 150$ km is the meridional domain size, $L_{\mathrm{Sh}} =$ 100 km is the zonal shelf length. There are many ways of specifying the eddy diffusivity κ (e.g., Gent and McWilliams 1990; Visbeck et al. 1997; Gent 2011). In the interest of simplicity, we use an empirically-selected constant $\kappa = 234$ m^2/s since this yields a good agreement with the across-shelf transport.

In addition to the eddy transport, there is a mean across-shelf transport that is maintained by the winds. Although the mean transport is not entirely wind driven, the Ekman transport far outweighs the contribution due to eddy momentum flux convergence (seen in Fig. 3a). To see this,

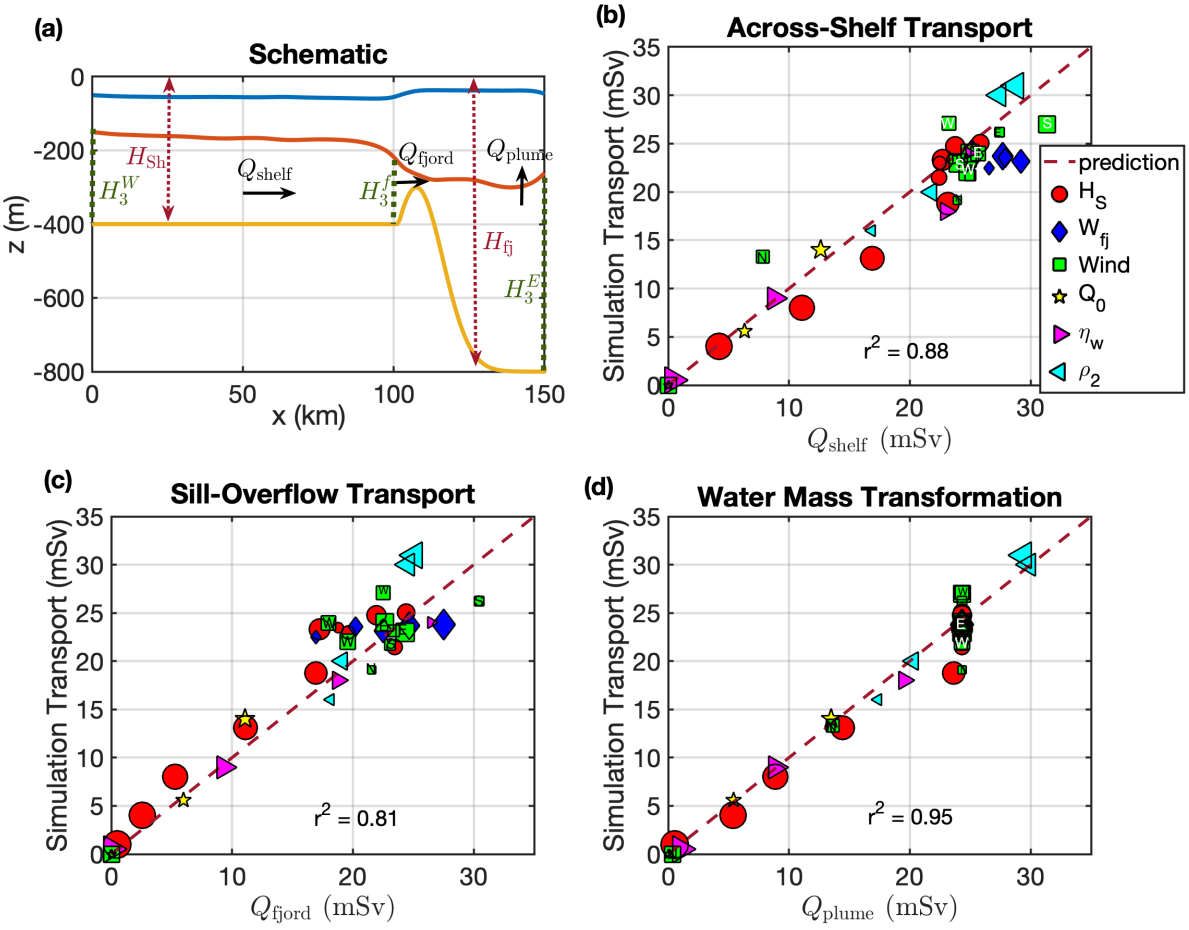

FIG. 9. (a) Schematic for the overturning circulation showing the three components of the shelf-to-glacier-face overturning. A comparison between the strength of the simulated overturning circulation diagnosed in the model and the predictions for onshore transport from: (b) Q_{shelf}, the sum of eddy and Ekman transports across the shelf given by Eqs. (10) and (13); (c) Q_{fjord}, the minimum of the geostrophic and hydraulically-controlled transports given by Eqs. (14),(15), and (17); and (d) Q_{plume}, the diabatic water mass transformation given by Eq. (18). Increasing marker sizes correspond to increasing values of each parameter with letter labels for varying wind direction.

we time-average and integrate the meridional momentum equation in Eq. (2a) vertically over all layers

$$C_d \overline{v}_3^2 \approx \frac{\tau_y}{\rho_1}, \tag{11}$$

i.e., that momentum input from the winds must be balanced in steady state by the momentum sink due to bottom friction. We combine Eq. (11) with the vertically-integrated meridional momentum equation in the bottom layer, which is approximately a balance between bottom friction and the Coriolis force

$$C_d \overline{v}_3^2 \approx -f \overline{h}_3 \overline{u}_3 . \tag{12}$$

This implies a time-mean bottom layer return flow $\overline{h}_3\overline{u}_3$, which can be shown to be equal and opposite to the top layer Ekman transport $U_{\text{Ek}} \equiv \overline{h}_1\overline{u}_1 = -\overline{h}_3\overline{u}_3$. Therefore the onshore top layer Ekman transport contribution to the mean overturning circulation is

$$Q_{\text{Ek}} = L U_{\text{Ek}} = L\tau_y(\rho_1 f)^{-1}, \tag{13}$$

where $L = 150$ km is the meridional domain length, and τ_y is the northward wind stress.

For the scenario where offshore Ekman return flow in the bottom layer exceeds the onshore eddy transport in the bottom layer, the bottom layer thickness vanishes at the fjord mouth, which results in a bottom layer transport, $Q_{\text{shelf}} = 0$, where the Ekman return flow transitions from the bottom layer to the intermediate layer such that $U_{\text{Ek}} \equiv \overline{h}_1\overline{u}_1 = -\overline{h}_2\overline{u}_2$. For the reference sill height H_S = 100 m, the theoretical prediction for a shutoff of AW

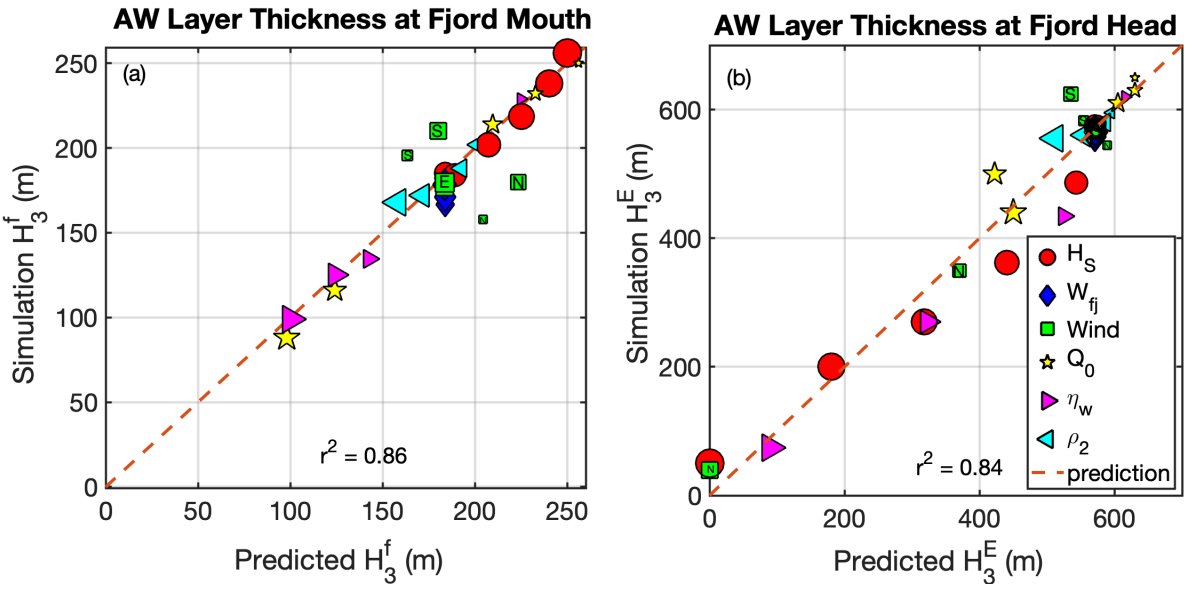

FIG. 10. A comparison between: (a) the simulated H_3^f (bottom layer thickness at x = 100 km, as labeled in Fig. 9a) and the predicted H_3^f from Eq. (22); (b) the simulated H_3^E (bottom layer thickness at x = 150 km, as labeled in Fig. 9a) and the predicted H_3^E from Eq. (20). Increasing marker sizes correspond to increasing values of each parameter with letter labels for varying wind direction.

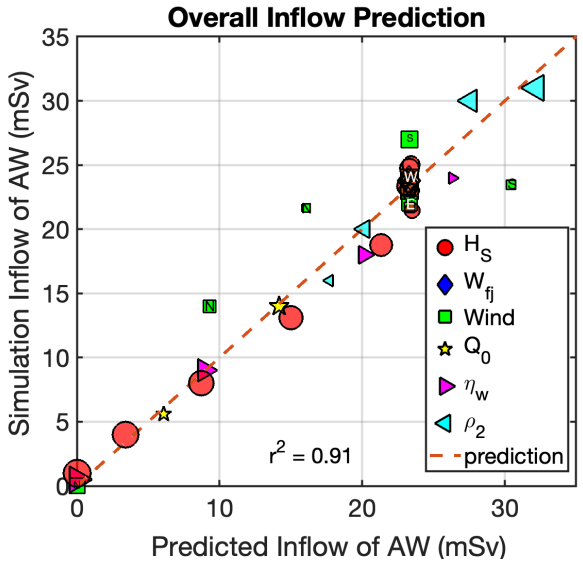

FIG. 11. A comparison between the strength of the simulation inflow of Atlantic Water diagnosed in the model to the predicted inflow (equivalent to bottom layer overturning circulation, Q_3) calculated from Eq. (23). Increasing marker sizes correspond to increasing values of each parameter with letter labels for varying wind direction.

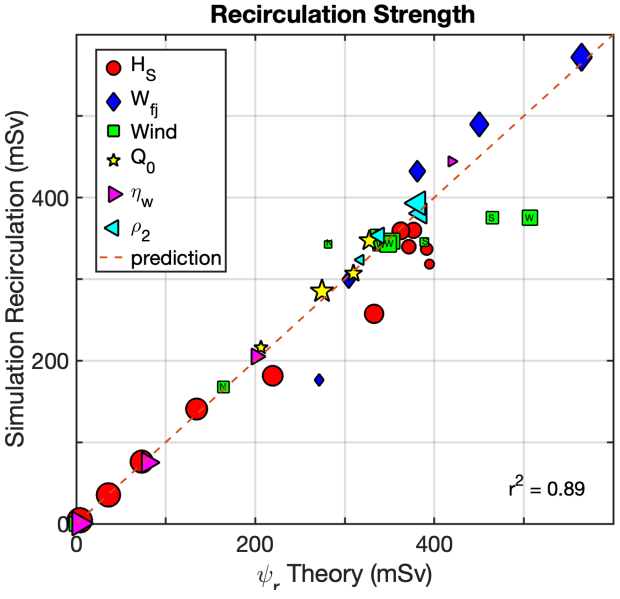

FIG. 12. A comparison between the strength of the simulation recirculation diagnosed in the model to the prediction for recirculation based on Eq. (28). Increasing marker sizes correspond to increasing values of each parameter with letter labels for simulations of varying wind direction.

access is achieved by a northward wind stress τ_y = 0.05 N/m^2; for the case of no sill, this is achieved by a northward wind stress τ_y = 0.08 N/m^2.

In Fig. 9b, we plot the overturning circulation strength diagnosed from the simulations compared to our the-

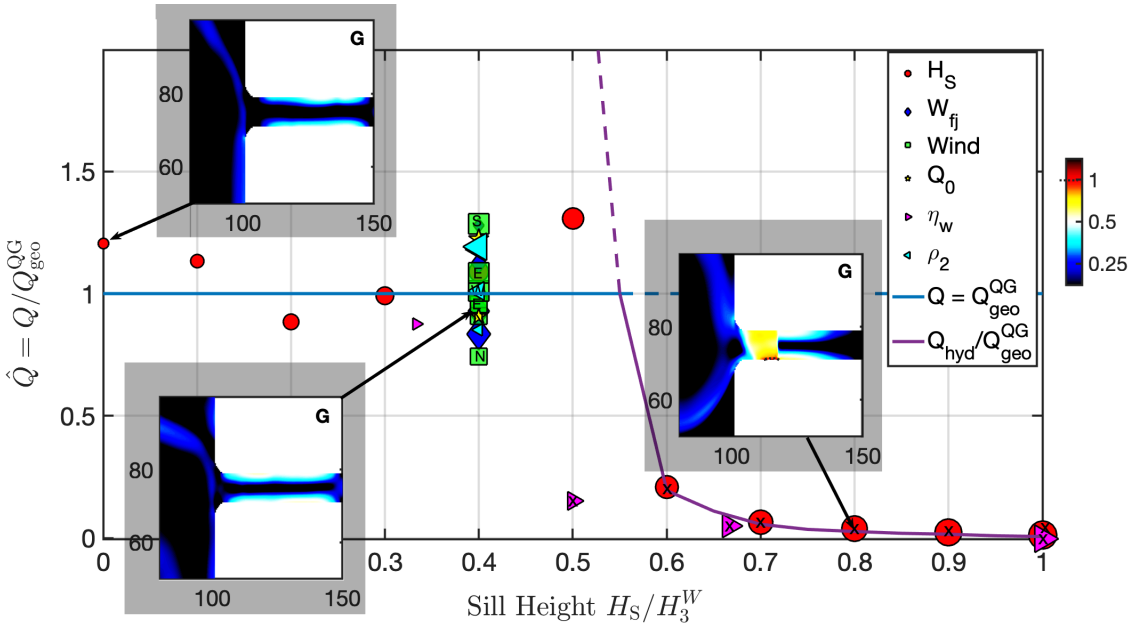

FIG. 13. Critical transport prediction using rotating 1-layer theory from Eq. (17) and simulation results both nondimensionalized by the geostrophic transport for varying nondimensionalized sill height. The solid lines show where the geostrophic and hydraulic-control theories set the bound on transport while the dashed lines do not (in accordance with Eq. (14)), which shows a transition to hydraulic control theory for $H_S/H_3^W > 0.55$. Insets show the composite Froude number G over a zoomed-in domain (x and y axes in km) centered on the fjord. Increasing marker sizes correspond to increasing values of each parameter with letter labels for simulations of varying wind direction. Experiments where G exceeds 0.8 at any location within the domain are marked with an 'x'.

ory for the bottom layer across-shelf transport $Q_{\text{shelf}} = \max(Q_{\text{eddy}} - Q_{\text{Ek}}, 0)$ using Eqs. (10) and (13). This theory predicts the across-shelf transport with a coefficient of determination of $r^2 = 0.88$.

b. Sill-Overflow Transport

The sill-overflow transport into the fjord is driven by the zonal isopycnal gradients in the AW depth η_2 outside the fjord relative to inside, which establishes a zonal pressure gradient along the fjord. This pressure gradient drives a (meridional) geostrophic flow within the fjord for smaller sill-overflow velocities, and becomes hydraulically-controlled for larger velocities (due to either taller sills or other parameters).

We present a prediction for both the geostrophic transport and critical transport (using hydraulic control theory) with the overall sill-overflow transport set by the minimum of the geostrophic and critical transport

$$Q_{\text{fjord}} = \min(Q_{\text{hyd}}, Q^{\text{QG}}_{\text{geo}}). \tag{14}$$

The rationale for this is that the flow is geostrophic (subcritical) if it is not hydraulically-controlled, and if the flow is hydraulically-controlled (necessarily evolving toward a critical flow in the steady state) the transport according to hydraulic control theory is the maximum achievable transport and is smaller than the geostrophic transport (Pratt and Whitehead 2007). This transition behavior from geostrophic to hydraulically-controlled flows is further discussed in Sect. 6a.

1) GEOSTROPHIC TRANSPORT

The across-sill (defined here as the zonal direction) geostrophic sill-overflow transport can be estimated based on the along-sill (meridional) geostrophic transport. This is based on the assumption that boundary currents in the fjord interior establish a zonal/along-fjord pressure head that is similar to the meridional/across-fjord pressure head within the fjord (Zhao et al. 2019). This is suggested in the bottom layer streamfunction from Fig. 3h, which shows a boundary current entering the fjord and flowing coherently across and along the sill. The pressure head across the boundary current in the along-sill and across-sill directions are thus similar values and representative of the geostrophic transport into the fjord.

The across-sill geostrophic transport (using the along-sill geostrophic transport as a proxy) is therefore based on the along-sill isopycnal gradient $H_3^{\text{f}} - H_3^{\text{E}} + (H_{\text{fj}} - H_{\text{Sh}})$,

and is derived using the quasigeostrophic (QG) approximation as

$$Q_{\text{geo}}^{\text{QG}} = \int H_3^M u_3 \, \mathrm{d}x' \approx \int H_3^M \left(\frac{g'_{5/2} H_2^M \partial_x \eta_2}{|f|(H_2^M + H_3^M)} \right) \mathrm{d}x'$$
$$\approx |f| L_{\text{d}}^2 (H_3^{\text{f}} - H_3^{\text{E}} + (H_{\text{fj}} - H_{\text{Sh}})), \tag{15}$$

where H_n^M is the mean reference thickness in each layer n (see Zhao et al. 2019 for further details).

2) HYDRAULICALLY-CONTROLLED TRANSPORT

When the geostrophic transport in the bottom layer is large enough, the velocity of the flow becomes comparable to the internal gravity wave speed. This occurs for a critical flow with respect to the composite Froude number $G = 1$, which may be defined as (Pratt and Whitehead 2007)

$$G^2 = \text{Fr}_1^2 + \text{Fr}_2^2 + \text{Fr}_3^2, \tag{16a}$$
$$\text{where } \text{Fr}_n = |\mathbf{u}_n| / \sqrt{g'_{n-1/2} h_n}, \tag{16b}$$

for g' defined in Eqs. (5a)-(5b) and $g'_{1/2} \equiv g$. Alternative definitions for the critical condition (e.g., Stern 1974) were tested, but did not lead to significant differences in our results.

This critical flow can be predicted using a variety of assumptions ranging from 1-layer rotating to multiple rotating layers. For simplicity, we use the 1-layer rotating solution for a hydraulically-controlled critical transport in the bottom layer (Whitehead et al. 1974),

$$Q_{\text{hyd}} = W_{\text{BC}} \sqrt{g'_{5/2}} \left(\frac{2}{3} \left[H_3^{\text{f}} - H_{\text{S}} - \frac{f^2 W_{\text{BC}}^2}{8 g'_{5/2}} \right] \right)^{3/2}. \tag{17}$$

Here, we assume the transport follows a boundary current of width $W_{\text{BC}} = \min(L_{\text{d}}, W_{\text{fj}})$, which is supported by our simulation results. We find that applying Eq. (17) is valid if Fr_3 dominates the Froude number in Eq. (16a). For tall enough sills, hydraulic control can occur in the top and middle layers (not shown), but this does not influence Q_3.

In Fig. 9c, we plot the overturning circulation strength diagnosed from the simulations vs. our theory for the sill-overflow transport Q_{fjord} as the minimum of the geostrophic and hydraulic transport (using Eqs. (14), (15), and (17)). This theory predicts the sill-overflow transport for each of the parameter variations with a coefficient of determination of $r^2 = 0.81$.

Although hydraulic control has been applied to many sill overflows in the open ocean (Pratt and Whitehead 2007), hydrographic measurements and numerical simulations support the existence of hydraulically-controlled flow within the Pine Island Glacier ice shelf cavity (Zhao et al. 2019; De Rydt et al. 2014), and outside the 79 North Glacier ice tongue cavity (Lindeman et al. 2020; Schaffer et al. 2020).

c. Diabatic Water Mass Transformation

The overturning circulation in steady state must be balanced by the near-glacier diabatic water mass transformation at the fjord head. Within the uniform density bottom layer, the theory for the vertical volume flux for a point source plume can be derived from classic self-similarity and entrainment assumptions as (Morton et al. 1956)

$$Q_{\text{plume}} = c_\varepsilon B_0^{1/3} (H_3^{\text{E}})^{5/3}, \tag{18}$$

where $c_\varepsilon = (6/5)(9/5)^{1/3} \pi^{1/3} \varepsilon^{4/3}$ (modified for a half-cone plume) for an experimentally-derived entrainment coefficient, $\varepsilon = .13$ (Linden 2000). The buoyancy flux $B = g'Q$ varies with depth, but is constant in the uniform density bottom layer $B_0 = g'_0 Q_0$, which is the buoyancy flux at the plume source (where $g'_0 = g(\rho_3 - \rho_0)/\overline{\rho}$). We can alternatively express this as a diabatic water mass transformation in terms of stratification and plume density (see Appendix A), which more clearly demonstrates how the overturning circulation may increase or decrease depending on the stratification and discharge strength due to the plume exit depth.

In Fig. 9d, we plot the overturning circulation strength diagnosed from the simulations compared to our theory for Q_{plume} in Eq. (18). This theory predicts the diabatic water mass transformation for each of the parameter variations with a coefficient of determination of $r^2 = 0.95$.

d. Piecing Together the Overturning Circulation

The bottom layer AW inflow is set by eddy-driven and Ekman transport in the continental shelf region, the minimum of the geostrophic transport and hydraulically-controlled transport in the fjord mouth sill region, and the plume-driven diabatic water mass transformation in the fjord head region. In order to make this prediction more comprehensive, we can equate the transport in these three regions and solve the system of equations to develop an a priori prediction of Q_3 without knowledge of the zonal isopycnal gradients in the continental shelf and fjord mouth sill regions. The bottom layer transport across the shelf-to-glacier-face domain can be summarized as

$$\max(\underbrace{Q_{\text{eddy}} - Q_{\text{Ek}}}_{Q_{\text{shelf}}}, 0) = Q_{\text{plume}} = \underbrace{\min(Q_{\text{hyd}}, Q_{\text{geo}}^{\text{QG}})}_{Q_{\text{fjord}}}. \tag{19}$$

If we equate $Q_{\text{plume}} = Q_{\text{shelf}}$ assuming that the bottom layer transport does not vanish, we can express H_3^{E} as

$$H_3^{\text{E}} = E^{-3/5} \left(\frac{\kappa W (H_3^{\text{W}} - H_3^{\text{f}})}{L_{\text{Sh}}} - \frac{L \tau_y}{\rho_1 |f|} \right)^{3/5}. \tag{20}$$

If all variables are known except H_3^{f} and H_3^{E}, we can solve the system of two equations that arise from equating

$Q^{\mathrm{QG}}_{\mathrm{geo}} = Q_{\mathrm{shelf}}$ and $Q_{\mathrm{hyd}} = Q_{\mathrm{shelf}}$ separately (Eq. (19)),

$$|f|L_{\mathrm{d}}^2\left(H_3^{\mathrm{f,geo}} - H_3^{\mathrm{E}}\right) + \frac{\kappa W}{L_{\mathrm{Sh}}} H_3^{\mathrm{f,geo}} = |f|L_{\mathrm{d}}^2(H_{\mathrm{Sh}} - H_{\mathrm{fj}}) + \frac{\kappa W H_3^{\mathrm{W}}}{L_{\mathrm{Sh}}} - \frac{L\tau_y}{\rho_1|f|}, \tag{21a}$$

$$W_{\mathrm{BC}}\sqrt{g'_{5/2}}\left(\frac{2}{3}\left[H_3^{\mathrm{f,hyd}} - H_{\mathrm{S}} - \frac{f^2 W_{\mathrm{BC}}^2}{8g'_{5/2}}\right]\right)^{3/2} + \frac{\kappa W}{L_{\mathrm{Sh}}} H_3^{\mathrm{f,hyd}} = \frac{\kappa W H_3^{\mathrm{W}}}{L_{\mathrm{Sh}}} - \frac{L\tau_y}{\rho_1|f|}, \tag{21b}$$

for $E \equiv c_\varepsilon (g'_0 Q_0)^{1/3}$. These two solutions ($H_3^{\mathrm{f,geo}}$ and $H_3^{\mathrm{f,hyd}}$) correspond to the water column thicknesses at the fjord mouth for the geostrophic ($Q^{\mathrm{QG}}_{\mathrm{geo}}$) and hydraulic-control (Q_{hyd}) overturning. Unfortunately, these relationships do not lend themselves easily to closed form solutions.

It can be shown that Q_{fjord} corresponds to the maximum H_3^{f}, defined as

$$H_3^{\mathrm{f}} = \max(H_3^{\mathrm{f,geo}}, H_3^{\mathrm{f,hyd}}), \tag{22}$$

due to Q_{eddy}, and thus Q_{shelf}, monotonically decreasing with increasing H_3^{f}. We can then solve for H_3^{E} using Eq. (20). In Fig. 10a, the simulation-diagnosed H_3^{f} is shown vs. the solution to Eq. (22), which predicts the simulation values with a coefficient of determination of $r^2 = 0.86$. In Fig. 10b, the simulation-diagnosed H_3^{E} is shown vs. the solution to Eq. (20), which predicts the simulation values with a coefficient of determination of $r^2 = 0.84$.

Thus, substituting H_3^{E} in Eq. (18) for Q_{plume} predicts the warm AW inflow as an explicit function of the input parameters in Sect. 3,

$$Q_3(H_3^{\mathrm{f}}, H_3^{\mathrm{E}}) = Q_3(H_{\mathrm{S}}, W_{\mathrm{BC}}, \tau_y, Q_0, H_3^{\mathrm{W}}, \rho_n). \tag{23}$$

This can also be evaluated using any of the formulas for the individual regions in Sects. 4a-c as a result of Eq. (19).

In Fig. 11, the simulation-diagnosed AW inflow is shown vs. the solution to Eq. (23). Even though predictions in each of the three individual regions are accurate separately (as shown in Fig. 9b-d), this comparison demonstrates that the overall prediction for the entire shelf-to-glacier-face theory predicts the AW inflow transport with a coefficient of determination $r^2 = 0.89$ and may be calculated a priori without knowledge of H_3^{f} and H_3^{E}. The theory provides a way to prognostically understand the role of each of the six parameters in the three regions (the continental shelf, the fjord mouth sill, and the fjord head) in setting the isopycnal gradients from the shelf to the glacier. This also provides a simple tool for guiding the interpretation of observations or estimation of parameters in Eq. (23) that may be difficult to observe.

5. Recirculation and Vorticity Balance

Although the overturning circulation is a critical component of the renewal of fjords and has received more attention in existing literature, the horizontal recirculation may play an equally important role in fjord dynamics and glacial melt rates. Specifically, recent work suggests that the near-glacier horizontal velocity, which owes its magnitude to the horizontal recirculation within the fjord, plays an important role in driving ambient front-wide glacial melt and may be comparable to the subglacial discharge-driven melt (Slater et al. 2018, Jackson et al. 2019). The importance of this contribution to melt rate is further discussed in Appendix B.

We approach the theory of horizontal recirculation strength using a recirculation region-integrated vorticity budget. We start with Eq. (2a) and multiply by thickness, h, and take the curl of the result to express the vorticity budget within each layer as

$$\underbrace{\partial_t \overline{\nabla \times h\mathbf{u}}}_{\text{tendency}} + \underbrace{\nabla \times (\nabla \cdot (\overline{h\mathbf{u}\mathbf{u}}))}_{\text{vort. advection}} - \underbrace{f\overline{\boldsymbol{\varpi}}}_{\text{vort. generation}} - \underbrace{\nabla \times (\overline{\mathbf{u}\boldsymbol{\varpi}})}_{\text{diapycnal advection}} = - \underbrace{\nabla \times \overline{h\nabla\phi}}_{\text{form stress curl}} - \underbrace{C_d \nabla \times \overline{|\mathbf{u}|\mathbf{u}}}_{\text{friction}}. \tag{24}$$

In the bottom layer, we find the dominant terms to be the diabatic vorticity generation, vorticity advection, and the bottom friction. Integrating Eq. (24) over the recirculation region, we find that the vorticity advection and diapycnal advection are each up to 15% of the magnitude of the other two terms and form stress curl and tendency are negligibly small (not shown). Therefore, our steady state balance may be roughly approximated by the diabatic vorticity generation, which spins up the bottom layer recirculation, and the bottom friction, which spins it down. This can be expressed as

$$\iint f\overline{\boldsymbol{\varpi}}\,\mathrm{d}A \approx \iint C_d \nabla \times \overline{|\mathbf{u}|\mathbf{u}}\,\mathrm{d}A. \tag{25}$$

We can simplify this relationship with a scaling argument for Eq. (25) in terms of the recirculation strength ψ_r and bottom layer transport Q_3. The time-average of Eq. (2b) implies that $\overline{\boldsymbol{\varpi}} = \nabla \cdot \overline{h\mathbf{u}}$ and by continuity, Q_3 equals the area integral of $\nabla \cdot \overline{h\mathbf{u}}$ in the diabatic region (a subregion of the bottom layer recirculation), so the left hand side of Eq. (25) is equal to fQ_3.

The right hand side of Eq. (25) (using Stokes' theorem) scales as

$$\iint C_d \nabla \times \overline{|\mathbf{u}|\mathbf{u}}\,\mathrm{d}A = \oint_{\partial A} C_d \overline{|\mathbf{u}|\mathbf{u}} \cdot \hat{\boldsymbol{\tau}}\,\mathrm{d}s \sim C_A C_d (\psi_r/(L_r H^E))^2, \tag{26}$$

where $\hat{\boldsymbol{\tau}}$ is a unit vector tangent to the boundary contour ∂A and s is the corresponding along-contour coordinate

over the gyre recirculation region A, and C_A is the circumference of the region A. Here, the mean velocity acted on by bottom friction scales as $\psi_r/(L_r H^E)$ for bottom friction concentrated in a boundary layer width L_r and near-glacier bottom layer thickness, H^E.

Thus, based on Eq. (25), we can make the following scaling argument

$$Q_3 f \sim C_A C_d \psi_r^2/(L_r H^E)^2 . \tag{27}$$

Based on our simulation results, L_r falls empirically between the boundary current width and the fjord half-width, $L_r \sim (L_\mathrm{d} + W_\mathrm{fj}/2)/2$. For narrow fjords $W_\mathrm{fj} < L_\mathrm{d}$, this empirical relationship fails and the recirculation boundary width likely fills the entire fjord half-width, $L_r \sim W_\mathrm{fj}/2$, which is untested due to resolution limitations. Therefore, for fjords of width L_d or larger, the scaling for recirculation strength is

$$\psi_r = \left(f(L_r H^E)^2 Q_3/(C_A C_d)\right)^{1/2} . \tag{28}$$

In Fig. 12, we compare the simulation recirculation strength to Eq. 28, which shows the theory predicts the bottom layer recirculation strength over varying parameters with a coefficient of determination of $r^2 = 0.87$. Additionally, if we assume a constant vorticity in the recirculation gyre, the maximum velocity v_max is approximately

$$v_\mathrm{max} \sim 2\psi_r/(L_r H^E) , \tag{29}$$

which is a useful parameter for the melt rate estimate further discussed in Sect. 7 and Appendix B.

6. Roles of Fjord Geometry and Variability

The simulation results in Sect. 3 and overturning and recirculation theory in Sects. 4 and 5 aim to capture many factors controlling fjord circulation. However, there are additional fjord circulation characteristics and phenomena that are potentially also important and deserve further investigation. First, we present an expanded discussion on the role of vertical and horizontal hydraulic control in fjord circulation and as a driver of intra-fjord variability. Following this, we diagnose the existence and role of low-frequency variability within the fjord and coastal currents in our simulations and subsequently, its high-frequency counterpart including submesoscale variability.

a. Transition to Hydraulic Control

In Sect. 4b, we applied simple theories for the transport in geostrophic and hydraulically-controlled flows. Although these simple theories fit our simulation results, the onset of hydraulic control in a complex fjord-to-shelf geometry (with both horizontal and vertical constrictions) in the presence of variability is not adequately addressed in the hydraulic-control theory literature and requires further discussion.

In Fig. 13, we highlight the transition from the geostrophic to the hydraulically-controlled regimes in our simulation results. We compare the diagnosed nondimensionalized transport ($\hat{Q} \equiv Q/Q^\mathrm{QG}_\mathrm{geo}$) to the geostrophic and hydraulic control theory predictions (Eqs. (15) and (17)), calculated as a function of nondimensionalized sill height ($H_\mathrm{S}/H_3^\mathrm{W}$). The subpanels show xy-plane maps of the composite Froude number G for three cases of varying sill height, with the hydraulically-controlled case exhibiting critical values of $G \approx 1$.

In the sensitivity experiments (Sect. 3), we varied each parameter individually relative to the reference case, but further regimes are possible when we co-vary parameters. Fig. 14 shows the nondimensionalized mean bottom layer transport ($\hat{Q} = Q/Q_\mathrm{geo}$) and its root-mean-square deviation as a function of nondimensionalized sill height (H_S/H_3^W) and fjord width ($W_\mathrm{fj}/L_\mathrm{d}$)for one such combination of parameters: co-varying sill height and fjord width. In this figure, for nondimensionalized sill heights above 0.5, the overturning circulation weakens, but for higher fjord widths, this critical sill height threshold increases to 0.9. Although the fjord widths tested in Sect. 3 are not narrow enough to permit hydraulically-controlled solutions, fjord width does lead to hydraulic control for taller sills, which is only apparent after co-varying sill height and fjord width.

The hydraulic control theory quantitatively captures the transport reduction in Fig. 14 for tall sills $H_\mathrm{S}/H_3^\mathrm{W} > 0.5$ and narrow fjords $W_\mathrm{fj}/L_\mathrm{d} < 1$. This also suggests the possibility that fjord width may lead to hydraulic control for sill heights $H_\mathrm{S}/H_3^\mathrm{W} < 0.5$, but requires narrower fjord widths. This is supported by the limitation of boundary current hydraulic control transport (Eq. (17)) on fjord width if it is narrower than the deformation radius. The transition to hydraulic control is also likely to vary for the covariation of other parameters, although this is untested.

The right panel in Fig. 14 shows that RMSD is greater for wider fjords, where shelf eddies can more easily penetrate into the fjord, and cases near hydraulic control, which reflects the observation that the regions of critical flow ($G \approx 1$) are also important sources of variability. This is due to the formation of isopycnal jumps/shocks with the same properties observed in Zhao et al. (2019), which have been shown to convert mean baroclinic and barotropic energy into eddy kinetic energy, and may be characterized as Kelvin-wave hydraulic shocks (Hogg et al. 2011).

b. Long-Term Variability and Periodic Flushing Events

In addition to variability on the shelf maintained by baroclinic instability (which leads to the across-shelf exchange, Q_eddy) and the variability generated at hydraulic

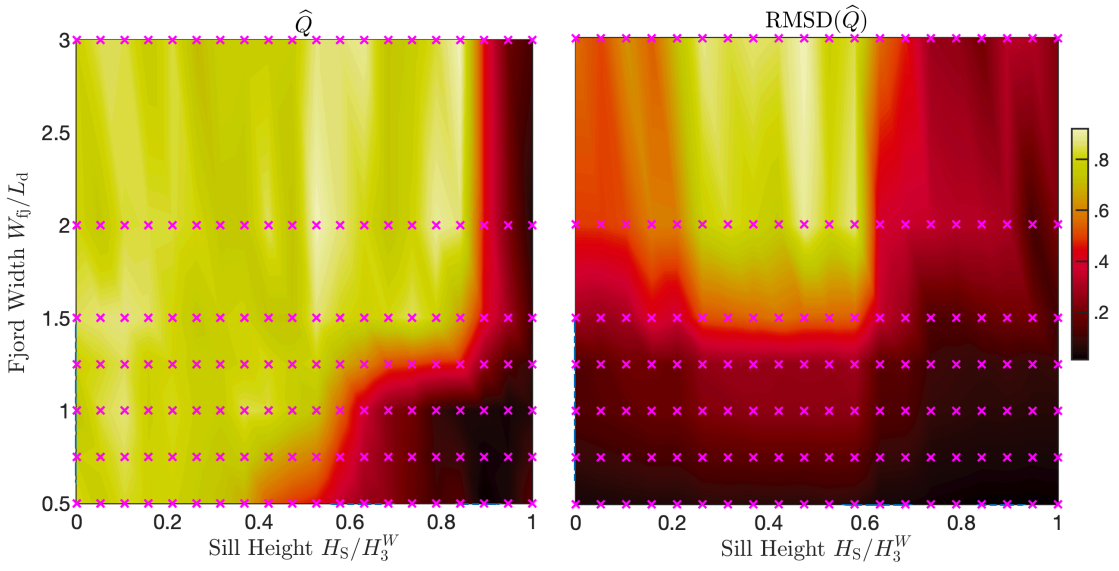

FIG. 14. Time-averaged (days 1300-1600) nondimensionalized bottom layer transport ($\hat{Q} = Q/Q_{\rm geo}$) and its root-mean-square deviation as a function of nondimensionalized sill height ($H_{\rm S}/H_3^{\rm W}$) and fjord width ($W_{\rm fj}/L_{\rm d}$). All other parameters are fixed to the reference case. Pink markers represent the geometric parameter combinations tested.

shocks near vertical/horizontal constrictions, we observe additional modes of variability.

Longer-term variability of the overturning circulation exists in our simulations and occurs simultaneously with perturbations in horizontal recirculation strength. To illustrate this, we show a time series of zonal transport using a Hovmöller plot for a $H_{\rm S} = 0$ m case in Fig. 15a,d,g in comparison with a $H_{\rm S}$ = 100 m case in Fig. 15b,e,h (with columns corresponding to layer). In these Hovmöller plots, the transport is integrated from y = 75 km to 79 km (inflow into northern half of the fjord) as a function of x and time, since it visually highlights the variability of recirculation and exchange near the fjord mouth. The right column (Fig. 15c,f,i) shows this northern half zonal transport profiled at the sill maximum (x = 107.5 km).

In the middle layer (Fig. 15d,e,f), we observe three cycles of a periodic flushing event on timescales of 60 days, which is approximately the residence timescale of the fjord, $\tau_r = W \times L \times H/Q$. This is particularly clear in the $H_{\rm S} = 150$ m case, where the sill is tall enough to influence the middle layer. In Fig. 15e, this periodic flushing appears as blue streaks representing westward outflow, which originate in the middle layer fjord interior as a disruption to the anticylonic recirculation and propagate across the shelf over a period of 20 days. The trend of the half-fjord transport at the sill-overflow in Fig. 15f also clearly shows a periodic signal on 60 day cycles for the $H_{\rm S} = 150$ m case (blue line). The bottom layer exhibits the same periodic signal, but is approximately 3 times weaker due to weak recirculation near the sill maximum since the main region of recirculation extends from x = 130 km to 150 km (whose magnitude also observably varies over a 60 day cycle in Fig. 15h). Fig. 15c,f,i shows that in general, the $H_{\rm S}$ = 0 m case has more short-term variability and the $H_{\rm S}$ = 150 m exhibits greater long-term variability.

The long-term variability (compared to the short-term) has a smaller contribution to the overall RMSD of the overturning circulation in the $H_{\rm S}$ = 0 case, but becomes increasingly important to consider for fjords with limited overturning and renewal.

The short-term variability accounts for most of the RMSD in Fig. 4 except for a few cases of weak overturning. This variability is apparent in Fig. 15 as the 1-2 day fluctuations in transport, although it is diagnosed differently. Within the fjord, this variability is dominated by coastally-trapped waves, which are generated either at the fjord mouth/sill maximum (due to the horizontal and vertical constriction) or the coastal current. The amplitude of the observed waves is larger for wider fjords, intermediate sill heights, stronger winds, stronger subglacial discharge, and larger zonal pressure gradients. The daily and monthly timescales of short-term and long-term variability, respectively, coexist in Fig. 15c,f,i.

c. Submesoscale Fjord Dynamics

The simulations presented so far span the non-eddying to weakly-eddying regime within the fjord. Although the eddy kinetic energy within the fjord is weak due to our choice of resolution, it does increase substantially for

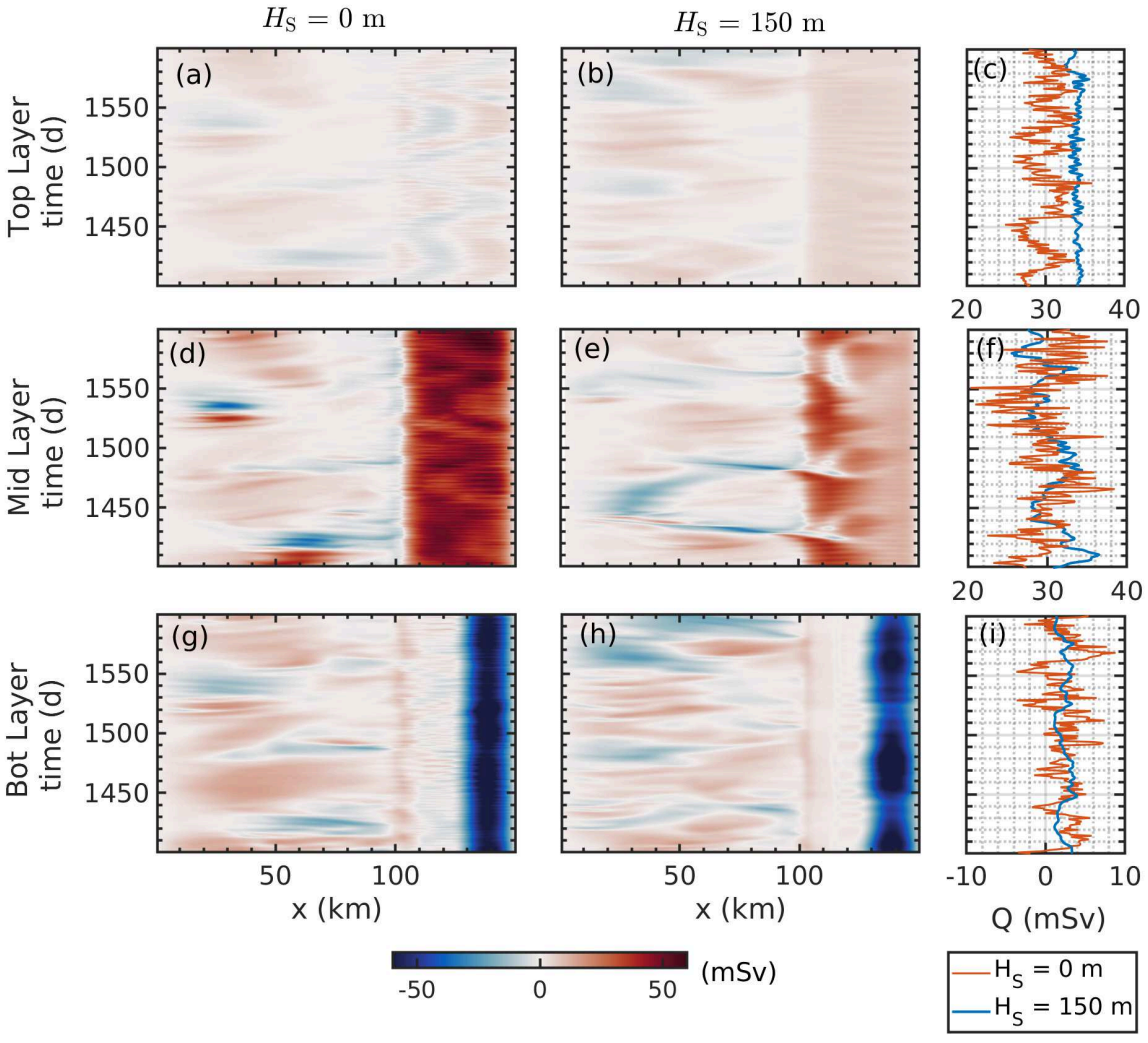

FIG. 15. (a)-(c) Top, (d)-(f) middle, and (g)-(i) bottom layer zonal transport Q calculated by integrating from y = 75 km (midline) to y = 79 km (northern fjord boundary). This is shown as a function of x for two cases of sill height: $H_S = 0$ m (left column) and $H_S = 150$ m (middle column) for the same fjord width $W_{fj} = 8$ km. The right column shows the timeseries of this half-fjord transport at $x = 107.5$ km (sill maximum). Periodic flushing events on timescales of 60 days (long-term variability) are more apparent for the $H_S = 150$ m case in the middle and bottom layers, while high frequency variability on timescales of 1-2 days is more apparent in the $H_S = 0$ m case, but also exists in the $H_S = 150$ m case.

high-resolution simulations of fjord-only domains. We find that although the total overturning strength and recirculation strength do not depend strongly on resolution ($\sim$20% increase for both from dl = 1000 m to dl = 68 m), submesoscale eddies do appear within fjords and the eddy contribution accounts for a significant proportion of the overturning circulation (up to 40% in the highest resolution cases).

In Fig. 16, a reference run at high resolution (dl = 68 m) with $H_S = 0$ m and $W_{fj} = 8$ km shows evidence of submesoscale activity. The submesoscale eddies in Fig. 16d-f have a peak vorticity of $\zeta/f \approx 4$ and diameters on the order of 1 km, which are small compared to the deformation radius. They are found to be primarily generated near the curved sidewall regions near the mouth of the fjord. These eddies influence both the mean along-fjord and across-fjord isopycnal gradients, as can be seen in Fig. 16a-c in comparison with the corresponding low-resolution case in Fig. 6a.

In the surfaces of interface depth (Fig. 16a-b), coastally-trapped waves (as previously discussed) appear to form isopycnal shocks within the fjord and near the coastal current. These waves and shocks propagate in the prograde direction and have shock amplitudes that decay from the

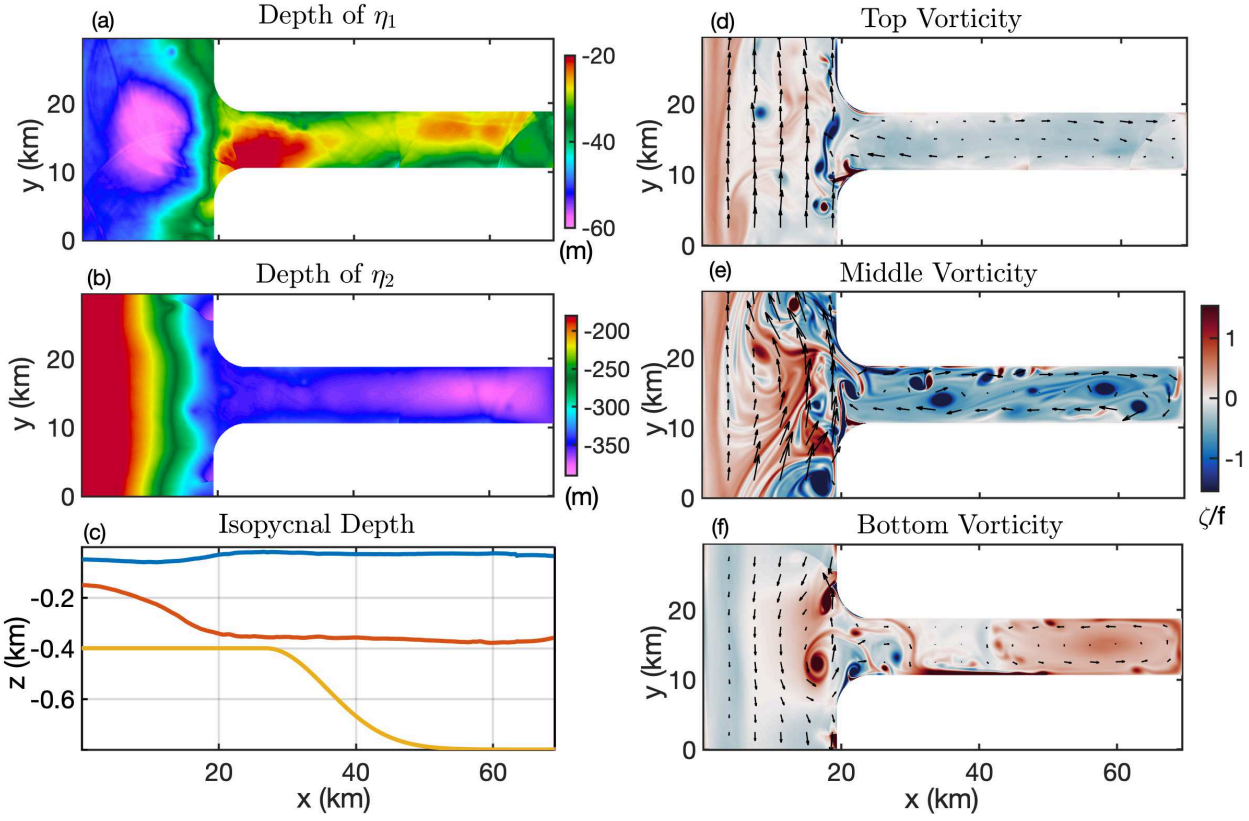

FIG. 16. High-resolution (dl = 68 m) simulation of a case with no sill and $W_{\rm fj} = 8$ km with snapshots of (a),(b) surfaces of interface depth η_1 and η_2 and (c) their along-midline depth ($y = 75$ km). (d)-(f) Snapshot of vorticity with velocity quivers for each layer (at day 200). The maximum velocities are 0.42, 0.66, 0.37 m/s in the top, middle, and bottom layers, respectively. See the supplemental material for a movie of this figure.

coast with a width $L_{\rm d}$ and are similar in behavior to the Kelvin wave hydraulic shocks discussed in Hogg et al. (2011). Interestingly, the bottom layer coastal eddies in Fig. 16f propagate in the same direction as the waves and shocks (northward/prograde), while the background coastal mean flow in this layer is southward. In both reality and models that permit such effects, these sources of variability may lead to elevated mixing in the fjord interior and variability of the recirculation and boundary current transport, which may be explored in a future study.

7. Discussion and Concluding Remarks

a. Summary

In glacial fjords, there is a complex interaction of dynamics in the shelf, fjord, and discharge/melt plumes, with multiple controls of the overturning circulation and horizontal recirculation (Straneo and Cenedese 2015; Carroll et al. 2017; Jackson et al. 2018). In this study, we examine the influence of key geometric controls (sill height, external stratification, and fjord width) on overturning in the shelf-to-glacial face system and horizontal recirculation in the fjord interior.

In Sect. 2, we discuss the idealized 3-layer numerical model setup to simulate the full shelf-to-glacial-face system. We examine the sensitivity of overturning and recirculation to six important parameters in Sect. 3 that capture variations in geometry (fjord width and sill height), boundary forcing (AW depth, winds, and subglacial discharge), and stratification. We find that the overturning and recirculation increase more significantly with decreasing sill height, deeper AW, and increasing subglacial discharge (shown in Figs. 4 and 5). Additionally, the horizontal recirculation significantly increases with fjord width.

We develop and test comprehensive theories that provide clarity on the role of each control in Sect. 4. The theory for the overturning circulation is pieced together using theories for the continental shelf, the fjord mouth sill, and the fjord head regions. The theory accurately predicts the simulated overturning over realistic ranges of each control parameter for each of the three regions and provides predictions for the AW layer thickness at the fjord mouth

and fjord head (Fig. 10), which can be used to predict the overall AW transport (Fig. 11). In Sect. 5, we develop a theory for the bottom-layer horizontal recirculation based on a vorticity balance between bottom friction and the diabatic vorticity generation of the water mass transformation, which accurately predicts the recirculation over realistic ranges of each control parameter (Fig. 12).

In Sect. 6 we discuss the modes of external and internal variability of the system. We further discuss hydraulic control at the fjord mouth and the role of both low-frequency and high-frequency variability on the shelf and within the fjord. The sill overflow can transition from geostrophic to hydraulically-controlled regimes with varying sill height, AW depth, and fjord width, and can explain the reduction in warm water inflow over realistic fjord parameters similarly to results from Zhao et al. (2019). Submesoscale variability was also observed in a configuration with a fjord attached to a smaller coastal shelf region shown in Fig. 16, and potentially plays an important role in the overturning and recirculation.

b. Glacial Melt Rate Implications

Using the theories we presented in Sects. 4 and 5 supported by the numerical simulations presented in Sect. 3, we can estimate glacial melt rates taking into account fjord circulation. The melt rate is predominantly dependent on two parameters: the vertical velocity of the discharge plume, which depends on discharge strength and the stratification set by open ocean and the overturning circulation, and the near-glacier horizontal velocity (the main driver of ambient melt), which depends on the strength of the horizontal recirculation.

Although we do not expect accurate estimates given the possible range of the empirical coefficients C_d and γ_T, it is still useful to provide melt rate estimates based on Eqs. (B1a) - (B2b) with horizontal and vertical velocities from our simulation results and theory, which we hope will guide future circulation-aware glacial melt rate parameterizations (further discussed in Appendix B). Our predicted maximum discharge plume-driven melt rate (or rate of undercutting) for Jakobshavn parameters is 8.7 m/day and the predicted ambient melt rate over the rest of the terminus in contact with the bottom layer AW is 1.1 m/day. However, due to its much larger area, the ambient melt accounts for 80% of the total volume melt and is $\sim$1.0 km^3/year based on a bottom layer thickness of 400 m and fjord width of 8 km (see Appendix B for further details). However, the freshwater input is still dominated by the discharge plume rather than meltwater, which supports our model assumptions of excluding the meltwater contribution to the buoyancy forcing in the fjord and supports recent findings that ambient melt driven by horizontal recirculation may be as important or more than the subglacial discharge-driven melt (Slater et al. 2018; Jackson et al. 2019).

The connection between overturning circulation, horizontal recirculation, and melt rates raises the possibility of a dynamical feedback, which is not simulated in our model and can be described as follows: stronger horizontal recirculation leads to stronger ice front velocities, which leads to higher melt rates by increasing turbulent transfer of heat to the ice face, which leads to stronger buoyancy forcing and thus, water mass transformation and overturning, which induces stronger horizontal recirculation to balance the vorticity budget. However, additional modeling and observations are needed to assess the importance of the melt-circulation feedback.

c. Caveats and Future Directions

Due to the limitations of a simplified model configuration, there are a number of caveats. These include the simplicity of geometry on the shelf, the lack of sea ice/melange/icebergs and surface buoyancy forcing in the fjord, the low-order representation of vertical structure in the ocean, and a lack of time-dependent buoyancy forcing (both the plume and open-ocean conditions). In general, the across-shelf transport is likely to be much more complicated than presented in this study, with canyons and remotely-generated coastal currents playing important roles (e.g., St-Laurent et al. 2013; Moffat et al. 2009), such that a more realistic across-shelf transport component of the theory is likely more complex. Also, tests of the inter-fjord separation distance (not shown) suggest that the strength of the coastal current is influenced by this parameter. Furthermore, since we only consider mixing due to the entrainment of the ambient and discharge plume, our theories assume that tides and sill overflows/bottom boundary layer processes are small contributions to the overall mixing. To account for this, the theory from Sect. 4 can be modified to include such contributions by replacing Q_{plume} with a total diabatic mixing term, $Q_{\text{diab}} = Q_{\text{plume}} + Q_{\text{tide}} + Q_{\text{BBL}}$. The overall overturning prediction in Eq. (23) can therefore by modified to include realistic parameterizations of Q_{tide} and Q_{BBL}. However, the potential importance of vertical mixing throughout the fjord to the overall overturning circulation remains an open question.

Following this study, there are a number of open questions that require further study. Additional work is needed to investigate the intra-fjord submesoscale phenomenology and the distribution of mixing within the shelf-to-glacial-face system and how it influences fjord renewal through both observations and modeling. Another future avenue would be to investigate the interaction between adjacent fjords. Also, a potential feedback exists between the fjord circulation and glacial melt rates (which controls

the strength of the diabatic forcing and thus, the circulation), but requires testing in a model that permits such a feedback. Finally, the boundary layer processes responsible for the melting at the glacial face requires both careful observational and modeling work in order to close the gap between our simple melt rate parameterizations based on plume and ice-ocean boundary layer theory and in-situ melt rate observations. In addition, measurements of fjord recirculation and spatial density variations at depth are lacking and are critically needed to compare with our findings in the hopes of improve our understanding of fjord circulation and their influence on glacial melt rates.

Acknowledgments. The authors would like to thank Pierre St-Laurent for allowing the use of the open source code BEOM and two anonymous reviewers for helpful comments. The model source code is available at **www.nordet.net/beom.html**. This material is based in part upon work supported by the National Science Foundation under Grants PLR-1543388 and OCE-1751386.

APPENDIX A

Plume Parameterization in an Isopycnal Model

We derive a point-source plume solution with a piecewise-constant background density, which can be used in isopycnal models such as BEOM. This is a special case of plume theory in a continously-stratified fluid (see e.g., Turner 1979).

The traditional theory of plumes with uniform background density predicts that buoyant plumes are largely controlled by the buoyancy forcing, which sets the entrainment and mixing of the plume with the ambient fluid (Morton et al. 1956). An axisymmetric turbulent plume can be defined based on the parameters B (buoyancy flux), z (height above the source), and R (radial length scale). For a constant background density, it is often assumed that the profiles are self-similar and dimensional analysis can be used to find the vertical velocity w, reduced gravity g', and R as a function of z.

The conservation of mass, momentum, and buoyancy flux can be written as (Turner 1979)

$$\frac{\partial m}{\partial z} = 2\alpha m/R, \tag{A1a}$$

$$\frac{\partial mw}{\partial z} = mg'/w, \tag{A1b}$$

$$\frac{\partial mg'}{\partial z} = -mN^2(z), \tag{A1c}$$

for a mass defined as $m = R^2 w$. For the specific case of piecewise-uniform density, the buoyancy flux (third equation) can be simplified to

$$B = mg'. \tag{A2}$$

B is constant within each layer, but changes at each interface according to this definition, which is discontinuous since g' is discontinuous. We implement a simple first-order Euler scheme for R and w, which converges for small interval size $\Delta z \sim 0.1$ m. We use this to solve for $R(z)$ and $g'(z) = B/m$ at each step in z. At interfaces, we solve for the jump in B and g' as $\Delta B = B_+ - B_-$ and $\Delta g' = g'_+ - g'_-$ before solving for m and w. These jumps are defined as

$$\Delta B = \pi R^2 w g(\rho_+ - \rho_-)/\bar{\rho}, \tag{A3a}$$

$$\Delta g' = g(\rho_+ - \rho_-)/\bar{\rho}. \tag{A3b}$$

This density of the plume can therefore be defined as

$$\rho_P(z) = -g'\bar{\rho}/g + \rho(z), \tag{A4}$$

which is continuous since

$$\rho_{P+} - \rho_{P-} = -(g'_+ - g'_-)\bar{\rho}/g + (\rho_+ - \rho_-) = 0. \tag{A5}$$

For the 3-layer isopycnal model, the overturning circulation is determined by buoyancy fluxes and mass entrainment driven by either a point source or line source. The mass flux and density flux relationships can be determined in multiple ways. Fig. A1 illustrates one way to partition control volumes to determine the overall bulk water mass transformations, which are defined in terms of the two unknowns: volume transport in the bottom and top layers, Q_3 and $-Q_1$. The volume transport in the middle layer must compensate the transport in the other two layers. The density flux conservation equations for the overall system can then be written as (with mass conservation already applied)

$$(Q_3 - Q_0)\rho_3 + Q_0\rho_0 = Q_3\rho_3^P, \tag{A6a}$$

$$Q_1\rho_1 + (Q_3 - Q_1)\rho_2 = Q_3\rho_3^P. \tag{A6b}$$

We can solve for the unknowns as

$$Q_3 = \frac{Q_0(\rho_3 - \rho_0)}{\rho_3 - \rho_3^P}, \tag{A7a}$$

$$Q_1 = \frac{Q_3(\rho_2 - \rho_3^P)}{\rho_2 - \rho_1}, \tag{A7b}$$

where ρ_3^P is found using Eq. (A4) evaluated at the interface between between layers 2 and 3.

We choose W_{nudg} and L_{nudg} to be the width and length of the nudging region. In our simulations, we define our nudging region to be 5 km so the diabatic flux is resolved and distributed over at least 10 grid points, whereas the

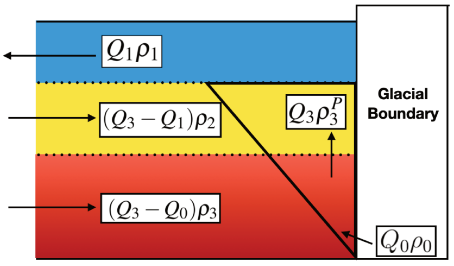

FIG. A17. A diagram of bulk water mass transport in our BEOM plume parameterization.

plume radius would be sub-gridscale. The thickness nudging due to plume entrainment corresponding to the diagram in Fig. A1 can be expressed as

$$\varpi_{1,\mathrm{p}} = \left(\frac{\partial h_1}{\partial t}\right)_{\mathrm{p}} = \frac{Q_1}{W_{\mathrm{nudg}} L_{\mathrm{nudg}}}, \tag{A8a}$$

$$\varpi_{2,\mathrm{p}} = \left(\frac{\partial h_2}{\partial t}\right)_{\mathrm{p}} = \frac{Q_3 + Q_0 - Q_1}{W_{\mathrm{nudg}} L_{\mathrm{nudg}}}, \tag{A8b}$$

$$\varpi_{3,\mathrm{p}} = \left(\frac{\partial h_3}{\partial t}\right)_{\mathrm{p}} = -\frac{Q_3 + Q_0}{W_{\mathrm{nudg}} L_{\mathrm{nudg}}}. \tag{A8c}$$

We can alternatively express Eq. (A7a) as two cases (depending on the plume exit depth),

$$Q_{\mathrm{plume}} = Q_3 = \begin{cases} Q_0(\rho_3 - \rho_0)(\rho_3 - \rho_3^P)^{-1}, & \text{if } \rho_3^P < \rho_2 \\ Q_0(\rho_3 - \rho_0)(\rho_3 - \rho_2)^{-1}, & \text{if } \rho_3^P \geq \rho_2 \end{cases} \tag{A9a}$$

$$\text{where } \rho_3^P = -g'_{5/2}\rho_2/g + \rho_3\,. \tag{A9b}$$

For the second case in Eq. (A9a), where $\rho_3^P \geq \rho_2$, the overturning circulation reduces to the Knudsen relations in the bottom two layers, which depends only on the stratification and the discharge strength. However, each of the parameters we consider can potentially lead to the first case ($\rho_3^P < \rho_2$), which decreases the overturning strength by a factor of $(\rho_3 - \rho_2)(\rho_3 - \rho_3^P)^{-1} < 1$. In the simulations discussed in Sect. 3, this was readily achieved for greater sill heights and deeper offshore AW, but this is also achievable for other parameters as well, especially a denser top layer and shallower fjord.

Similarly, a line plume parameterization with varying source width is implemented and test in our model. For a small discharge width (50 m or less), there is a negligible difference between the terminal volume flux of a point plume and line plume parameterization. For larger plume source widths, the overturning strength and neutral depth of the plume are quantitatively different, but the overturning still varies proportionally to the discharge.

APPENDIX B

Circulation-Aware Glacial Melt Rate Estimates

An important implication for fjord overturning and horizontal recirculation is the submarine melt rate implied by our simulation results and theory. The purpose of this appendix is to draw a posteriori melt rate inferences from the overturning and recirculation strengths diagnosed from our simulations. We calculate the melt rates using a front-wide ambient melt (including a line plume) in the warm bottom layer area in contact with the glacial face as well as the melt rate within the half-cone subglacial discharge-driven plume over a much smaller area of the glacial face.

All along the glacial face, the melt rate per unit area can be solved using a combination of the depth-dependent plume equations (discussed in Appendix A) and the three-equation system (Hellmer and Olbers 1989; Holland and Jenkins 1999), which describes the thermodynamical equilibrium at the ice-ocean interface. This equilibrium can be expressed using approximate heat and salt conservation and the linearized freezing temperature of seawater,

$$q(L_i + c_i(T_b - T_i)) = \gamma_T c_w (T_p - T_b) \tag{B1a}$$

$$qS_b = \gamma_S (S_p - S_b)\,, \tag{B1b}$$

$$T_b = \lambda_1 S_b + \lambda_2 + \lambda_3 z\,. \tag{B1c}$$

Here, q (m s^{-1}) is the glacial melt rate per unit area, $L_i = 3.35 \times 10^5$ J kg^{-1} is the latent heat of fusion of ice, $c_w = 3.974 \times 10^3$ J kg^{-1} K^{-1} is the specific heat capacity of water, $c_i = 2 \times 10^3$ J kg^{-1} K^{-1} is the specific heat capacity of ice, T_p and S_p are the plume temperature and salinity, $T_i = -10$ °C is the ice temperature, T_b and S_b are the boundary layer temperature and salinity, γ_T and γ_S are the turbulent thermal and salt transfer coefficient, and $\lambda_1 = -5.73 \times 10^{-2}$ °C psu^{-1}, $\lambda_2 = 8.32 \times 10^{-2}$ °C, and $\lambda_3 = 7.61 \times 10^{-4}$ °C m^{-1} are the freezing point slope, offset, and depth. These empirical values are consistent with those used in previous studies (Sciascia et al. 2013; Cowton et al. 2015).

Although previous parameterizations of the turbulent transfer coefficients used constant values (Hellmer and Olbers 1989), more recent work shows that a dependence on ocean velocities near the boundary are in better agreement with submarine melt rate measurements (Jenkins et al. 2010)

$$\gamma_T = C_d^{1/2} \Gamma_T \sqrt{v^2 + w^2}\,, \tag{B2a}$$

$$\gamma_S = C_d^{1/2} \Gamma_S \sqrt{v^2 + w^2}\,, \tag{B2b}$$

where $C_d = 2.5 \times 10^{-3}$ is the drag coefficient, $\Gamma_T = 2.2 \times 10^{-2}$ and $\Gamma_S = 6.2 \times 10^{-4}$ are the thermal and salt transfer constants, and v and w are the tangential horizontal and vertical velocities at the glacier boundary. For our simulations, the plume vertical velocity (at 100 m above the

discharge source) ranges from 0 m/s (no subglacial discharge) to 3.7 m/s (greatest discharge) and the horizontal velocity $v = v_{\max}$ in the gridpoint adjacent to the glacier face in the lower layer ranges from 0.05 to 0.3 m/s.

Although the vertical velocities (in the plume) are much larger than the horizontal velocities near the glacial face, recent work suggests that the ambient melt dynamics driven by the horizontal recirculation may be as important as the subglacial discharge-driven melt (Slater et al. 2018, Jackson et al. 2019). This is partly due to the fact that ambient melt affects a much larger area of the glacial face. Studies have also noted that ambient melt rates from the plume melt parameterizations are unrealistically low compared to the total ice flux at the terminus, but have not determined which melt processes produce these high melt rates (Jackson et al. 2019; Straneo and Cenedese 2015; Carroll et al. 2016; Fried et al. 2015).

For Jakobshavn Glacier, using a subglacial discharge of 1700 m^3/s (based on assuming all runoff enters as subglacial discharge in Beaird et al. 2017), our theory predicts an overturning circulation of 85 mSv and horizontal recirculation strength of 300 mSv. Here, the plume vertical velocity at the mid-depth point of the bottom layer (predicted to be 440 m thick) is 2.7 m/s and the horizontal velocity at the glacier boundary is 0.34 m/s. Using a bottom layer ambient temperature and salinity of 4 ^{o}C and 34.0 psu (Gladish et al. 2015), we can calculate the plume temperature and salinity at mid-depth in the bottom layer. Using Eqs. (B1a)-(B1c), this allows us to find the boundary layer temperature and salinity and the melt rates. Our predicted maximum discharge plume-driven melt rate (or rate of undercutting) is 8.7 m/day and the predicted ambient melt rate over the rest of the terminus in contact with the bottom layer AW is 1.1 m/day. However, due to its much larger area, the ambient melt accounts for 80% of the total volume melt and is $\sim$1.0 km^3/year based on a bottom layer thickness of 400 m and fjord width of 8 km.

We note that the ambient melt rate is dictated by $v_{\max}$, since it is $\sim$30 times larger than the vertical velocity of the distributed line plume predicted by plume theory (Jenkins 2011). Thus, the ambient melt rate including the horizontal velocity is approximately 30 times larger than the one using only the vertical line plume velocity. Since our melt rate estimate uses the discrete density profile from our 3-layer model and is only an approximation to the realistic vertical structure of temperature and salinity, it is only able to capture an approximate bulk melt rate estimate.

The ratio of areas covered by the discharge plume and ambient melt plume depends on the mean width of the discharge plume source and the vertical rise distance. The mean width for a point/cone plume is half of its radius at neutral buoyancy ($R_{\max}/2$) and for a truncated-line plume with a finite width w_s discharge source, the mean width is the mean of w_s and $R_{\max}/2$ (Cowton et al. 2015, Jackson et al. 2017). For a truncated-line plume of $w_s = 200$ m at the source (which best fits Greenland's fjords, as shown in Jackson et al. 2017), our simulation results for the Jakobshavn test case suggests a subglacial discharge plume that occupies $\sim$3% of the surface area of the face, but accounts for 20% of the meltwater supply. However, the buoyancy forcing is likely dominated by the freshwater from subglacial discharge rather than the meltwater production.

Recently, it has been argued that the empirical coefficients C_d and Γ_T are untested in tidewater glaciers and larger values are more consistent with observations, i.e. $C_d = 1 \times 10^{-2}$, $\Gamma_T = 4.4 \times 10^{-2}$, which would result in melt rate estimates that are 4 times greater (Jackson et al. 2019).

References

Bamber, J. L., A. J. Tedstone, M. D. King, I. M. Howat, E. M. Enderlin, M. R. van den Broeke, and B. Noel, 2018: Land Ice Freshwater Budget of the Arctic and North Atlantic Oceans: 1. Data, Methods, and Results. *J. Geophys. Res. Oceans*, **123 (3)**, 1827–1837, doi:10.1002/2017JC013605.

Bartholomaus, T. C., and Coauthors, 2016: Contrasts in the response of adjacent fjords and glaciers to ice-sheet surface melt in West Greenland. *Ann. Glaciol.*, **57 (73)**, 25–38, doi:10.1017/aog.2016.19.

Beaird, N., F. Straneo, and W. Jenkins, 2017: Characteristics of Meltwater Export from Jakobshavn Isbrae and Ilulissat Icefjord. *Ann. Glaciol.*, **58 (74)**, 107–117, doi:10.1017/aog.2017.19.

Carroll, D., D. A. Sutherland, E. Shroyer, J. D. Nash, G. Catania, and L. A. Stearns, 2017: Subglacial discharge-driven renewal of tidewater glacier fjords. *J. Geophys. Res. Oceans*, **122**, 6611–6629.

Carroll, D., and Coauthors, 2016: The impact of glacier geometry on meltwater plume structure and submarine melt in greenland fjords. *Geophys. Res. Lett.*, **43 (18)**, 9739–9748, doi:10.1002/2016GL070170.

Chu, V. W., 2014: Greenland ice sheet hydrology: A review. *Progress in Physical Geography: Earth and Environment*, **38 (1)**, 19–54, doi:10.1177/0309133313507075.

Cook, A. J., P. R. Holland, M. P. Meredith, T. Murray, A. Luckman, and D. G. Vaughan, 2016: Ocean forcing of glacier retreat in the western Antarctic Peninsula. *Science*, **353 (6296)**, 283–286.

Cowton, T., D. Slater, A. Sole, D. Goldberg, and P. Nienow, 2015: Modeling the impact of glacial runoff on fjord circulation and submarine melt rate using a new subgrid-scale parameterization for glacial plumes. *J. Geophys. Res. Oceans*, **120**, 796–812.

De Rydt, J., P. R. Holland, P. Dutrieux, and A. Jenkins, 2014: Geometric and oceanographic controls on melting beneath Pine Island Glacier. *J. Geophys. Res. Oceans*, **119**, 2420–2438, doi:10.1002/2013JC009513.

Fraser, N. J., M. E. Inall, M. G. Magaldi, T. W. N. Haine, and S. C. Jones, 2018: Wintertime Fjord-Shelf Interaction and Ice Sheet Melting in Southeast Greenland. *J. Geophys. Res. Oceans*, **123 (12)**, 9156–9177, doi:10.1029/2018JC014435.

Fried, M. J., G. A. Catania, T. C. Bartholomaus, D. Duncan, M. Davis, L. A. Stearns, J. Nash, E. Shroyer, and D. Sutherland, 2015: Distributed subglacial discharge drives significant submarine melt at

a greenland tidewater glacier. *Geophys. Res. Lett.*, **42 (21)**, 9328–9336, doi:10.1002/2015GL065806.

Gent, P. R., 2011: The Gent–McWilliams parameterization: 20/20 hindsight. *Ocean Modelling*, **39 (1)**, 2–9, doi:https://doi.org/10.1016/j.ocemod.2010.08.002.

Gent, P. R., and J. C. McWilliams, 1990: Isopycnal Mixing in Ocean Circulation Models. *J. Phys. Oceanogr.*, **20 (1)**, 150–155, doi:10.1175/1520-0485(1990)020⟨0150:IMIOCM⟩2.0.CO;2.

Gladish, C. V., D. M. Holland, A. Rosing-Asvid, J. W. Behrens, and J. Boje, 2015: Oceanic Boundary Conditions for Jakobshavn Glacier. Part I: Variability and Renewal of Ilulissat Icefjord Waters, 2001–14. *J. Phys. Oceanogr.*, **45 (1)**, 3–32, doi:10.1175/JPO-D-14-0044.1.

Griffies, S., and R. Hallberg, 2000: Biharmonic friction with a Smagorinsky-like viscosity for use in large-scale eddy-permitting ocean models. *Mon. Wea. Rev.*, **128**, 2935–2946.

Hellmer, H. H., and D. J. Olbers, 1989: A two-dimensional model for the thermohaline circulation under an ice shelf. *Antarctic Science*, **1 (4)**, 325–336, doi:10.1017/S0954102089000490.

Hogg, A. M., W. K. Dewar, P. Berloff, and M. L. Ward, 2011: Kelvin wave hydraulic control induced by interactions between vortices and topography. *J. Fluid Mech.*, **687**, 194–208, doi:10.1017/jfm.2011.344.

Holland, D. M., and A. Jenkins, 1999: Modeling Thermodynamic Ice-Ocean Interactions at the Base of an Ice Shelf. *J. Phys. Oceanogr.*, **29 (8)**, 1787–1800, doi:10.1175/1520-0485(1999)029⟨1787:MTIOIA⟩2.0.CO;2.

Inall, M. E., T. Murray, F. R. Cottier, K. Scharrer, T. J. Boyd, K. J. Heywood, and S. L. Bevan, 2014: Oceanic heat delivery via Kangerdlugssuaq Fjord to the south-east Greenland ice sheet. *J. Geophys. Res. Oceans*, **119 (2)**, 631–645, doi:10.1002/2013JC009295.

Jackson, R., J. Nash, C. Kienholz, D. Sutherland, J. Amundson, R. Motyka, D. Winters, E. Skyllingstad, and E. Pettit, 2019: Meltwater intrusions reveal mechanisms for rapid submarine melt at a tidewater glacier. *Geophys. Res. Lett.*, doi:10.1029/2019GL085335.

Jackson, R. H., S. J. Lentz, and F. Straneo, 2018: The Dynamics of Shelf Forcing in Greenlandic Fjords. *J. Phys. Oceanogr.*, **48 (11)**, 2799–2827, doi:10.1175/JPO-D-18-0057.1.

Jackson, R. H., E. L. Shroyer, J. D. Nash, D. A. Sutherland, D. Carroll, M. J. Fried, G. A. Catania, T. C. Bartholomaus, and L. A. Stearns, 2017: Near-glacier surveying of a subglacial discharge plume: Implications for plume parameterizations. *Geophys. Res. Lett.*, **44 (13)**, 6886–6894, doi:10.1002/2017GL073602.

Jakacki, J., A. Przyborska, S. Kosecki, A. Sundfjord, and J. Albretsen, 2017: Modelling of the Svalbard fjord Hornsund. *Oceanologia*, **59 (4)**, 473–495, doi:https://doi.org/10.1016/j.oceano.2017.04.004.

Jenkins, A., 2011: Convection-Driven Melting near the Grounding Lines of Ice Shelves and Tidewater Glaciers. *J. Phys. Oceanogr.*, **41 (12)**, 2279–2294, doi:10.1175/JPO-D-11-03.1.

Jenkins, A., P. Dutrieux, S. Jacobs, S. McPhail, J. Perrett, A. Webb, and D. White, 2010: Observations beneath Pine Island Glacier in West Antarctica and implications for its retreat. *Nat. Geosci.*, **3**, 468–472.

Lee, T., D. E. Waliser, J.-L. F. Li, F. W. Landerer, and M. M. Gierach, 2013: Evaluation of CMIP3 and CMIP5 Wind Stress Climatology Using Satellite Measurements and Atmospheric Reanalysis Products. *J. Climate*, **26 (16)**, 5810–5826, doi:10.1175/JCLI-D-12-00591.1.

Lindeman, M. R., F. Straneo, N. J. Wilson, J. M. Toole, R. A. Krishfield, N. L. Beaird, T. Kanzow, and J. Schaffer, 2020: Ocean Circulation and Variability Beneath Nioghalvfjerdsbrae (79 North Glacier) Ice Tongue. *J. Geophys. Res. Oceans*, **125 (8)**, e2020JC016091, doi:10.1029/2020JC016091.

Linden, P. F., 2000: *Convection in the environment. In Perspectives in Fluid Dynamics, ed. GK Batchelor, HK Moffat, MG Worster.* Cambridge University Press, Cambridge, U.K., 289 – 345 pp.

Magorrian, S. J., and A. J. Wells, 2016: Turbulent plumes from a glacier terminus melting in a stratified ocean. *J. Geophys. Res. Oceans*, **121 (7)**, 4670–4696, doi:10.1002/2015JC011160.

Moffat, C., 2014: Wind-driven modulation of warm water supply to a proglacial fjord, Jorge Montt Glacier, Patagonia. *Geophys. Res. Lett.*, **41 (11)**, 3943–3950, doi:10.1002/2014GL060071.

Moffat, C., B. Owens, and R. C. Beardsley, 2009: On the characteristics of Circumpolar Deep Water intrusions to the west Antarctic Peninsula Continental Shelf. *J. Geophys. Res. Oceans*, **114 (C5)**, doi:10.1029/2008JC004955.

Morlighem, M., and Coauthors, 2017: BedMachine v3: Complete Bed Topography and Ocean Bathymetry Mapping of Greenland From Multibeam Echo Sounding Combined With Mass Conservation. *Geophys. Res. Lett.*, **44 (21)**, 11,051–11,061, doi:10.1002/2017GL074954.

Morton, B. R., G. I. Taylor, and J. S. Turner, 1956: Turbulent gravitational convection from maintained and instantaneous sources. *Proceedings of the Royal Society of London. Series A. Mathematical and Physical Sciences*, **234 (1196)**, 1–23, doi:10.1098/rspa.1956.0011.

Pörtner, H. O., and Coauthors, 2019: IPCC, 2019: IPCC Special Report on the Ocean and Cryosphere in a Changing Climate. In press.

Pratt, L. J., and J. A. Whitehead, 2007: *Rotating Hydraulics*. Springer.

Pritchard, H. D., and D. G. Vaughan, 2007: Widespread acceleration of tidewater glaciers on the Antarctic Peninsula. *J. Geophys. Res. Earth Surf.*, **112 (F3)**, 1–10, doi:10.1029/2006JF000597.

Rignot, E., S. Jacobs, J. Mouginot, and B. Scheuchl, 2013: Ice-Shelf Melting Around Antarctica. *Science*, **341 (6143)**, 266–270, doi:10.1126/science.1235798.

Schaffer, J., T. Kanzow, W. von Appen, L. von Albedyll, J. E. Arndt, and D. H. Roberts, 2020: Bathymetry constrains ocean heat supply to Greenland's largest glacier tongue. *Nat. Geosci.*, **13**, 227–231, doi:10.1038/s41561-019-0529-x.

Sciascia, R., F. Straneo, C. Cenedese, and P. Heimbach, 2013: Seasonal variability of submarine melt rate and circulation in an East Greenland fjord. *J. Geophys. Res. Oceans*, **118**, 2492–2506.

Seroussi, H., M. Morlighem, E. Rignot, E. Larour, D. Aubry, H. Ben Dhia, and S. Kristensen, 2011: Ice flux divergence anomalies on 79 North Glacier, Greenland. *Geophys. Res. Lett.*, **38**, L09501, doi:10.1029/2011GL047338.

Slater, D. A., F. Straneo, S. B. Das, C. G. Richards, T. J. W. Wagner, and P. W. Nienow, 2018: Localized Plumes Drive Front-Wide Ocean Melting of A Greenlandic Tidewater Glacier. *Geophys. Res. Lett.*, **45 (22)**, 12,350 – 12,358, doi:10.1029/2018GL080763.

Spall, M. A., R. H. Jackson, and F. Straneo, 2017: Katabatic Wind-Driven Exchange in Fjords. *J. Geophys. Res. Oceans*, **122 (10)**, 8246–8262, doi:10.1002/2017JC013026.

St-Laurent, P., 2018: Back of Envelope Ocean Model (BEOM). URL www.nordet.net/beom.html, accessed 1 April 2018.

St-Laurent, P., J. M. Klinck, and M. S. Dinniman, 2013: On the Role of Coastal Troughs in the Circulation of Warm Circumpolar Deep Water on Antarctic Shelves. *J. Phys. Oceanogr.*, **43 (1)**, 51–64, doi:10.1175/JPO-D-11-0237.1.

Stern, M., 1974: Comment on rotating hydraulics. *Geophys. Fluid Dyn.*, **6 (2)**, 127–130, doi:10.1080/03091927409365791.

Stewart, K., A. Hogg, S. Griffies, A. Heerdegen, M. Ward, P. Spence, and M. England, 2017: Vertical resolution of baroclinic modes in global ocean models. *Ocean Modelling*, **113**, 50–65, doi:https://doi.org/10.1016/j.ocemod.2017.03.012.

Straneo, F., and C. Cenedese, 2015: The Dynamics of Greenland's Glacial Fjords and Their Role in Climate. *Annu. Rev. Mar. Sci.*, **7 (1)**, 89–112, doi:10.1146/annurev-marine-010213-135133.

Straneo, F., and P. Heimbach, 2013: North Atlantic Warming and the Retreat of Greenland's Outlet Glaciers. *Nature*, **504 (7478)**, 36–43, doi:https://doi.org/10.1038/nature12854.

Sutherland, D. A., R. H. Jackson, C. Kienholz, J. M. Amundson, W. P. Dryer, D. Duncan, E. F. Eidam, R. J. Motyka, and J. D. Nash, 2019: Direct observations of submarine melt and subsurface geometry at a tidewater glacier. *Science*, **365 (6451)**, 369–374, doi:10.1126/science.aax3528.

Turner, J. S., 1979: *Buoyancy effects in fluids. Cambridge University Press Paperback.* 368 pp.

Visbeck, M., J. Marshall, T. Haine, and M. Spall, 1997: Specification of Eddy Transfer Coefficients in Coarse-Resolution Ocean Circulation Models. *J. Phys. Oceanogr.*, **27 (3)**, 381–402, doi:10.1175/1520-0485(1997)027⟨0381:SOETCI⟩2.0.CO;2.

Whitehead, J. A., A. Leetmaa, and R. Knox, 1974: Rotating hydraulics of strait and sill flows. *Geophysical Fluid Dynamics*, **6 (2)**, 101–125, doi:10.1080/03091927409365790.

Wood, M., E. Rignot, I. Fenty, D. Menemenlis, R. Millan, M. Morlighem, J. Mouginot, and H. Seroussi, 2018: Ocean-Induced Melt Triggers Glacier Retreat in Northwest Greenland. *Geophys. Res. Lett.*, **45 (16)**, 8334–8342, doi:10.1029/2018GL078024.

Xu, Y., E. Rignot, D. Menemenlis, and M. Koppes, 2012: Numerical experiments on subaqueous melting of Greenland tidewater glaciers in response to ocean warming and enhanced subglacial discharge. *Ann. Glaciol.*, **53 (60)**, 229–234.

Zhao, K. X., A. L. Stewart, and J. C. McWilliams, 2019: Sill-Influenced Exchange Flows in Ice Shelf Cavities. *J. Phys. Oceanogr.*, **49 (1)**, 163–191, doi:10.1175/JPO-D-18-0076.1.

Name	*Parameter*	*Test Cases*	*Ilulissat estimate*	*Units*
Sill Height	H_S	[0:25:250]	100	m
Fjord Width	W_{fj}	[4,6,8,12,16,24]	8	km
Fjord Length and Depth (constant)	$L_{fj} \times H_{fj}$	50×0.8	47×0.75	km
Wind Magnitude and Direction	τ_x, τ_y	[0, 0.015, 0.03, 0.1] $\times$ [N,S,E,W]	$\sim$0.03 $\times$ [N,S,E,W]	N/m^2
Subglacial Discharge	Q_0	[0, 100, 250, 500, 1000, 2000]	$\sim$1700	m^3/s
Atlantic Water Depth	η_2^W	[-100, -150, -200, -250, -300]	$\sim$-150 $\pm$ 50	m
Stratification	$\rho_3 - \rho_2$	[0.3, 0.4, 0.5, 0.6, 0.7]	$\sim$0.5	kg/m^3

TABLE B1. Summary of key fjord parameters and test cases for the numerical simulations and their corresponding estimates for Ilulissat Icefjord in West Greenland. All variables are independently varied relative to the reference case in Sect. 3c except fjord length and depth. The estimates of Ilulissat fjord properties are based on data from Gladish et al. (2015) and Beaird et al. (2017).